Summer 7-15-2019

Experimental Investigation of Steady-state and Transient Flow Boiling Critical Heat Flux

Soon Kyu Lee

Soon Kyu Lee
Candidate

Nuclear Engineering
Department

This thesis is approved, and it is acceptable in quality and form for publication:

Approved by the Thesis Committee:

Anil Prinja, Chairperson

Youho Lee

Amir Ali

Nicholas Brown

EXPERIMENTAL INVESTIGATION OF STEADY-STATE AND TRANSIENT FLOW BOILING CRITICAL HEAT FLUX

by

SOON KYU LEE

BACHELOR OF SCIENCE IN MECHANICAL ENGINEERING
PURDUE UNIVERSITY, 2014
MASTER OF SCIENCE IN MECHANICAL ENGINEERING
PURDUE UNIVERSITY, 2015

THESIS

Submitted in Partial Fulfillment of the
Requirements for the Degree of

Master of Science
Nuclear Engineering

The University of New Mexico
Albuquerque, New Mexico

July, 2019

ACKNOWLEGEMENTS

I would like to acknowledge the following people who have helped me through my journey towards higher education in nuclear engineering. First, I would like to appreciate my advisor, Dr. Youho Lee for his invaluable guidance and support. His dedication to conducting research inspired me to have a profound appreciation in engineering and science. He taught me the value of communication to effectively share the accomplished work. I am grateful for the support and involvement of my advisory committee members Dr. Anil Prinja, Dr. Amir Ali, and Dr. Nicholas Brown.

I would also like to thank my colleague Dr. Maolong Liu for his guidance. He initiated my interest in research of flow boiling heat transfer and helped me with the groundwork this thesis. Moreover, I would like to thank Dr. Edward Blandford and Dr. Maolong Liu for their contribution to the construction of the flow boiling loop and funding from Idaho National Laboratory. I acknowledge the Department of Energy's Nuclear Engineering University Program (NEUP) and Integrated Research Project (IRP) for funding the research.

Finally, I would like to dedicate this work to my wife and parents for their unwavering love and support. Their encouragement kept me pursue higher goals in my life.

EXPERIMENTAL INVESTIGATION OF STEADY-STATE AND TRANSIENT FLOW BOILING CRITICAL HEAT FLUX

By

Soon K. Lee

B.S. Mechanical Engineering, Purdue University, 2014

M.S. Mechanical Engineering, Purdue University, 2015

ABSTRACT

The Critical Heat Flux (CHF) causes a rapid reduction of heat transfer coefficient with a rapid increase of cladding temperature, which may induce physical failure of the heated material. Understanding CHF phenomena and reliable prediction of the boiling behavior are needed to design a heat transfer system including nuclear reactors. Due to the complex nature of CHF, it is still an active research topic of interest. With an increasing interest in Accident Tolerant Fuel (ATF), CHF of ATF is essential topic of study for the detailed design of the fuel – cladding element and for the reactor safety analysis.

In this study, flow boiling experiments were conducted at atmospheric pressure with deionized water in an internal-tubular channel with a uniformly heated surface. With this heat flux controlled system, steady-state and transient CHF experiments were performed to gain a mechanistic understanding of the boiling nature. The experiments

were conducted under the following conditions: (1) mass flux, G of 200 kg/m^2s - 2000 kg/m^2s, (2) inlet subcooling of 54℃, 34℃, and 10℃, (3) atmospheric pressure of 84 kPa. Experiments at low mass flux were repeated on the same specimen to observe the effect of the surface characteristic change on CHF. Despite the notable changes in surface wettability and roughness, change in flow CHF was not observed, which implies the limited significance of surface characteristic on CHF under flow condition. To mechanistically understand observed CHF differences among the tested materials, material thermal parameters were considered. In addition, a statistical approach was made to analyze CHF differences among the tested materials covering a wide range of mass flow rate, which demonstrated a reducing relative CHF differences with increasing mass flow rate. It implies limited significance of material-sensitivity for the design of fuel and cladding and steady-state safety. Yet, observed CHF differences at low mass flux require a more detailed thermal-hydraulic material-sensitivity study at it may play an immense role under the accident scenarios where mass flow is limited. Lastly, transient boiling CHF experiments were carried out to enhance cladding behavior with a pulsed power insertion under flow condition. With measurable values from the transient boiling experiments, boiling curve construction method is presented.

TABLE OF CONTENTS

LIST OF FIGURES

LIST OF TABLES

CHAPTEER 1: INTRODUCTION

1.1 Background

Currently, zirconium-based alloys are mainly used as the cladding for Light Water Reactors (LWRs). Zirconium-based alloys have attractive qualities in the perspective of neutron economy and thermal-hydraulics. Yet, under severe accident zirconium cladding rapidly reacts with steam at high temperature, generating hydrogen gas as follows [1]:

$$\mathrm{Zr} + 2\mathrm{H}_2O \rightarrow ZrO_2 + 2H_2 \quad (1.1)$$

This reaction occurred in the Boiling Water Reactors (BWRs) of the Fukushima Daiichi Nuclear Power Plant. Hydrogen gas was released into the reactor maintenance unit, resulting explosion severely damaging the plant. Following the Fukushima accident, the U.S. Department of Energy Office of Nuclear Energy (DOE-NE) initiated Advanced Fuels Campaign (AFC) to develop Accident Tolerance Fuel (ATF) and cladding materials for an extended accident coping time [2]. For cladding concepts, nuclear grade iron-chromium aluminum (FeCrAl) [3], silicon carbide fiber-reinforced silicon carbide ceramic composite (SiCf/SiC) [4], and chromium-coated Zircaloy are considered. Candidate ATF concept FeCrAl has an advantage over the zirconium-based cladding in the reactor safety perspective, as it has meaningfully slower reaction kinetics in high-temperature steam [3]. FeCrAl alloy has enhanced mechanical failure limit compared to the zirconium-based cladding [5]. FeCrAl alloy also showed stable irradiation tolerance [6], adequate rupture and ballooning behaviors [5,7]. The disadvantage of the FeCrAl cladding is that it absorbs more neutron compared to the zirconium-based cladding, harming the neutron economy in a reactor. Therefore, thinner cladding thickness with

increased uranium enrichment in fuel elements is needed to recover for the neutron economy in case of the cladding replacement [8]. ATF research has successfully gained an enhanced understanding of the material performance; yet, there has been the limited evaluation of FeCrAl from a thermal-hydraulics perspective. Understanding of the thermal-hydraulics behavior of FeCrAl alloy including Critical Heat Flux (CHF) is required for fuel and cladding design, as well as the reactor safety analysis. Due to limited understanding from the thermal-hydraulics perspective, ATF researches adopt similar fuel designs and fuel pin power level using standard CHF correlations [9-16].

CHF describes the thermal-hydraulic limit where the heated surface leading sudden phase change of coolant. Sudden reduction of heat transfer due to inefficient cooling from the vapor layer causes localized overheating of the heated surface. There are two types of boiling crisis in flow boiling condition. Under low heat flux condition, the flow goes through slug and annular flow to reach liquid dry out, which is a boiling crisis that causes rapid temperature overshoot of the heating material, leading to a high-quality flow. Under high heat flux condition, vapor generation rate is high enough in the nucleate boiling regime to establish a vapor micro-layer film near the heating wall. This vapor micro-layer is formed under the liquid film and separates the liquid film from the heating wall to cause Departure of Nucleate Boiling (DNB), hence it is low-quality flow. In this study, experimentally measured CHF is the CHF by DNB. Thermal-hydraulic analysis of CHF is crucial for fuel and cladding design purpose, as it sets the limit of the operating condition of the nuclear reactor.

Addition to the steady-state CHF data, transient CHF research is another informative data to support reactor safety. The rapid temperature rise of the nuclear fuel

cladding during Reactivity Insertion Accidents (RIAs) increases the temperature gradient of the fluid micro-layer, initiating an increased number of active nucleation sites [17,18]. Increased number of active nucleation site effectively enhances heat transfer and delays CHF, as demonstrated by several flow CHF experiments [19-22]. Still, due to the lack of transient CHF model, fuel temperature prediction during RIAs utilizes steady-state CHF models [23], which were developed on steel-base materials. For mechanistic fuel failure analysis during transience, further investigation of cladding flow boiling behavior including transient CHF is needed.

The Groeneveld CHF lookup table [24] is widely used in reactor thermal hydraulics codes (i.e., RELAP 5-3D and COBRA-TF). Yet, the CHF lookup table is developed using steel materials, not Zircaloy. While it is believed that the effect of materials on CHF is limited, studies have revealed the impact of the heater material on the boiling heat transfer, highlighting the effect of surface characteristics [25,26]. Pool boiling studies showed an increase in CHF with an increase in surface wettability, surface roughness and porosity [25-28]. Moreover, studies on surface characteristics were further improved with the use of nano-fluid, which showed enhanced boiling heat transfer [29,30]. Most of the surface effect studies were carried out under pool boiling condition; therefore, investigation under flow boiling condition is needed. Few studies showed apparent CHF differences in pool boiling environments for ATF cladding concepts, including SiC and FeCrAl alloys [25, 31], which suggests CHF may also vary under flow boiling conditions. Therefore, this study investigates experimental steady-state and transient CHFs of various tube materials including FeCrAl (Fe-13Cr-6Al or C36M and Fe-12Cr-6Al-2Mo or C26M2) alloys.

1.2 Objectives

Flow boiling experiments were performed to help gain a mechanistic understanding of flow CHF. Experimental steady-state CHFs were measured for FeCrAl alloy, Zircaloy, and other metal-based materials under identical flow condition to impartially compare CHF attendants. Thermal-hydraulic performance of candidate ATF material FeCrAl alloy is established and compared to other tube materials.

Analysis effort is completed to gain an understanding of observed different CHFs for the tested materials with consideration of macroscopic material parameters including surface characteristics and material thermal parameters. In addition, steady-state CHF experiments were conducted in a wide range of mass flux to statistically investigate the relationship between different CHFs among tested materials and mass flux.

Experimental transient CHFs were measured and compared to that of steady-state. Transient boiling behavior of cladding materials with respect to the pulsed power insertion is analyzed in detail. With an understanding of the transient boiling behavior and measurable values, the transient boiling curve construction method is provided.

CHAPTER 2. EXPERIMENTAL METHOD

2.1 Flow Boiling Experimental Test Facility

The flow boiling facility was constructed and operated by the University of New Mexico's thermal hydraulics and reactor safety laboratory. The flow boiling loop is designed to perform internal flow boiling experiments investigating various implications on both steady-state and transient CHFs under flow condition.

2.1.1 Test Loop Configuration

The flow boiling test loop consists of a fluid reservoir separating steam and fluid, a heat exchanger, a circulation pump, a heater, an orifice flow meter, a power supply, a data acquisition system, temperature and pressure instrumentation, and the test section. The deionized water is used as the working fluid in this experiment. The objective of this experimental facility is to measure both steady-state and transient flow boiling heat transfer phenomena and to collect the critical heat flux data points from different tube materials with a wide range of mass flow rate and inlet subcooling.

A fluid reservoir stores working fluid and separates heated liquid and gas coming out from the test section. Heat exchanger cools down heated water from the fluid reservoir before it goes to the circulation pump. A pump generates a wide range of mass fluxes from 200 kg/m^2s to 4000 kg/m^2s, which is measured by the orifice flow meter installed on a pipe prior to the test section. The cooled down working fluid from the

pump gets heated by the heater to adjust inlet subcooling of the fluid entering the test section. The working fluid enters the test section in an upward direction. The entire loop is made of SS316 to minimize corrosion and is insulated with the steam-resistant high-temperature fiberglass insulation tubes to minimize heat loss to the environment.

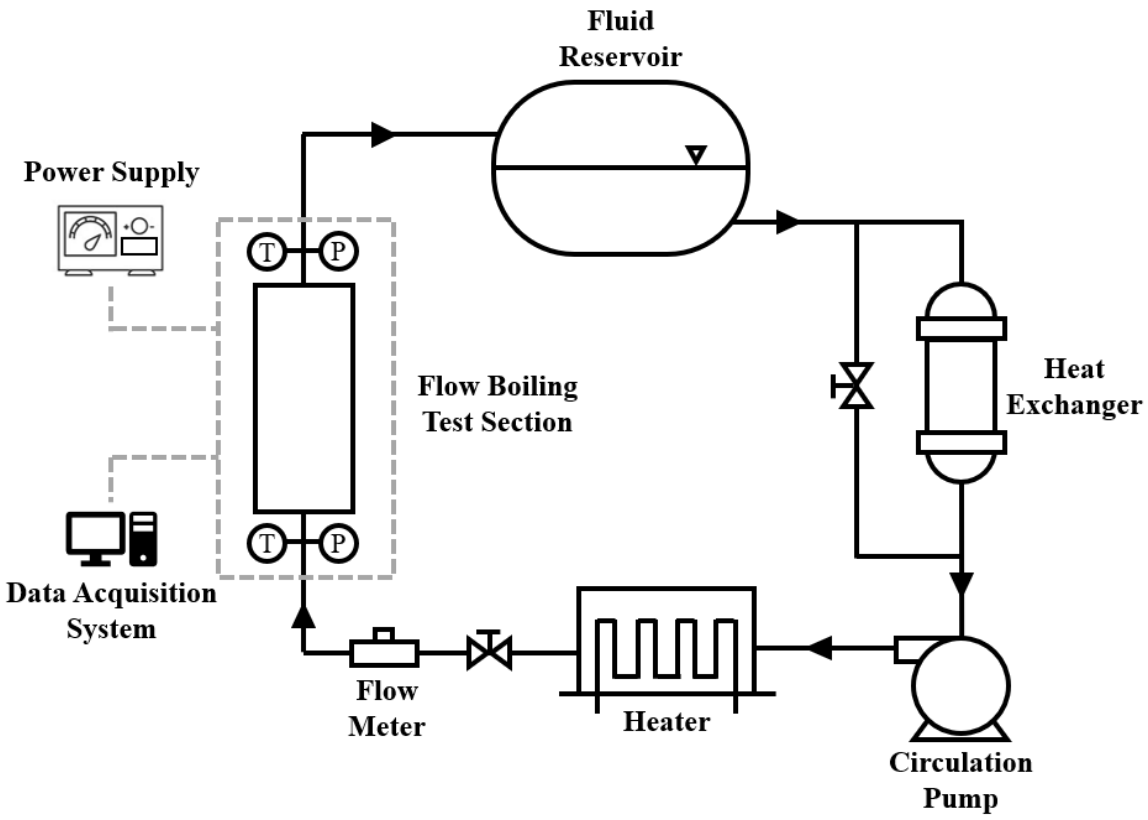

Figure 2.1 Schematic of the flow boiling test loop

2.1.2 Test Section

A detailed cross-sectional view of the test section is shown in Fig 2.2. The test section consists of a 50.8 cm (20 inch) long test tube, copper power terminals, current and

voltage transducers. The entire test section is covered with the steam-resistant high-temperature fiberglass insulation tubes.

Test tubes with 9.525 mm (3/8 inch) outer diameter are connected to the flow loop. Prior to the heated length, 25.4 cm long insulated pipe length is provided to generate fully-developed flow. Maximum required entrance length in this study was 24 cm for 8.763 mm inner diameter tube under the mass flux of 2000 $\mathrm{kg/m^2 s}$. The entrance length is evaluated by the following equation:

$$\mathrm{L_{entrance}} \approx 4.4 \cdot Re^{\frac{1}{6}} \cdot D_{tube} \tag{2.1}$$

The test section is heated by the direct current power supply (Magna Power, TSA16-1200) via copper power terminals. The heated length of the test tube is 5.08 cm (2 inch) to maximize the power available from the power supply.

K-type thermocouples with a diameter of 0.05 mm (0.002 inch) (Delta M Corp.) and 0.25 mm (0.01 inch) (Omega, SA1-K) were installed on the outer surface of the heated length to measure the surface temperature and to detect the temperature overshoot from the CHF occurrence. For steady-state experiments, a thermocouple was attached near the top end of the heated length, approximately ~5 mm apart from the upper power terminal. For transient experiments, a thermocouple was attached on the middle of the heated length, 2.54 cm apart from the upper power terminal. It is designed to simplify the transient CHF detection and calculation as actual CHF location is unlikely to place near the top end of the heated length due to fast transience.

Copper power terminals were carefully machined; yet, surface contacting the test tube is not perfectly smooth. Moreover, commercially manufactured test tubes have rough surfaces. Due to rough surfaces of copper terminals and test tubes, the junction

between the power terminals and test tubes does not have perfect contact. Nickel-silver compound was applied on the junction to enhance the smooth direct current transition from the power terminal to the test tube. Moreover, the applied compound prevented heat generation from the contact resistance and maximized contact conductance.

Under the current test setup, minimal heat loss though insulation is detected by taking temperature measurement of the outer surface of the insulation material. Yet, the negligible temperature increase throughout the whole experiment was less than 4℃.

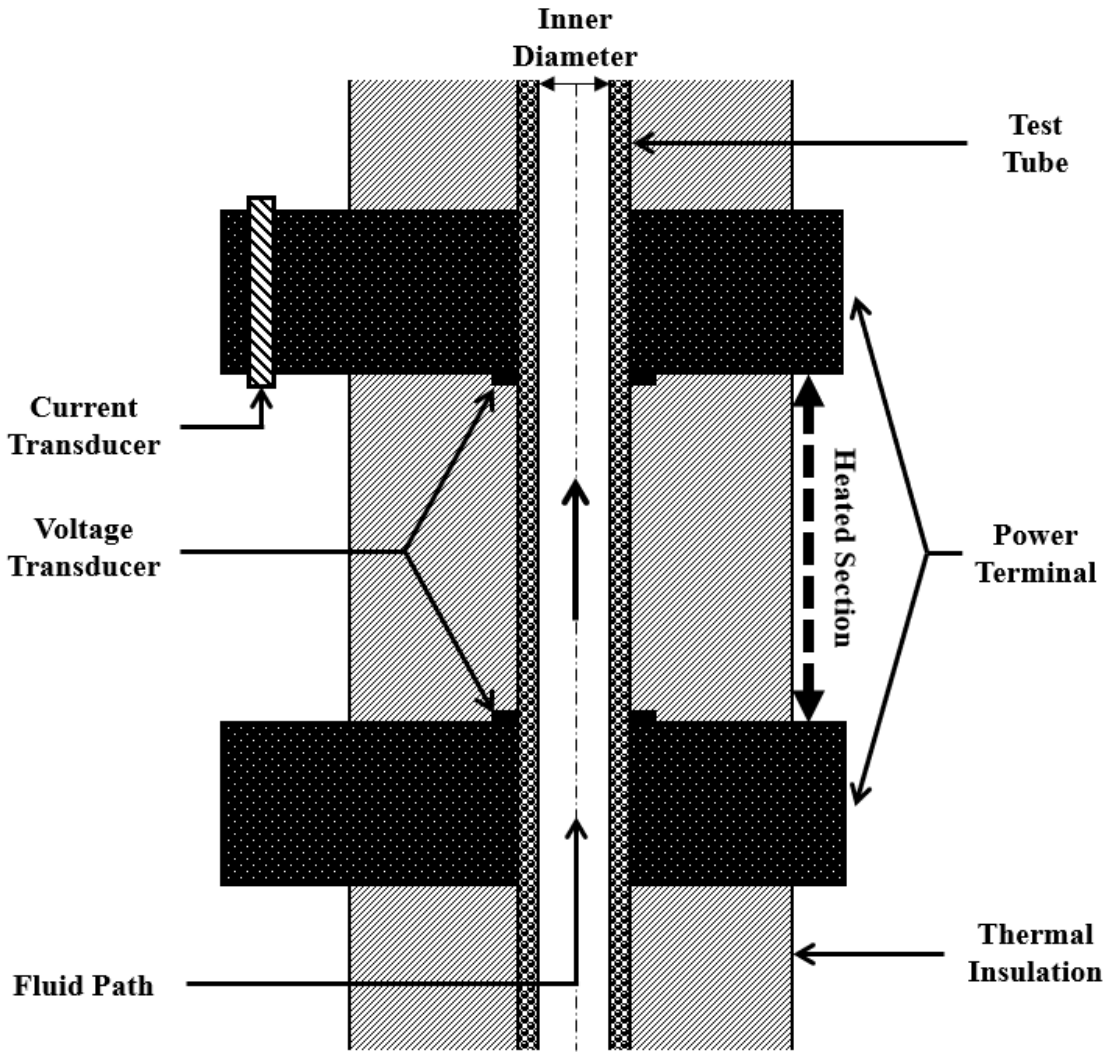

Figure 2.2 Cross-sectional view of the test section

2.1.3 Data Acquisition System

Temperature, pressure, flow, voltage and current data were measured using National Instrument isothermal terminal blocks (NI-9212). Labview is used to acquire data and to control power supply. With ~2 milliseconds load transient response provided from the power supply, power supply was shut off upon the CHF occurrence, which was detected by the temperature overshoot. Rapid shut down of the power supply prevented burn-out or failure of the test specimen for multiple CHF experiments. Yet, above the mass flux of 800 kg/m^2s, most of the test tubes failed even with rapid power supply shut down due to high heat flux. The data acquisition rate was 30Hz and 50Hz for steady-state and transient experiments, respectively.

2.2 Experiment Condition and Uncertainty

2.2.1 Experimental Operating Conditions

In steady-state critical heat flux study, flow boiling experiments were conducted at fixed inlet temperatures (54℃, 34℃, and 10℃ inlet subcooling) and mass fluxes (200 kg/m^2s to 2000 kg/m^2s) under atmospheric pressure on various tube materials including FeCrAl (C36M and C26M2) accident tolerant fuel cladding alloy, Inconel600, Monel400, Stainless Steel (SS304 and SS316), Grade 2 Titanium, and Zircaloy-4 with internal upward flow. Direct current power was incremented at 30 - 40 second intervals

until CHF is reached, which is detected by the temperature overshoot from the measured outer surface temperature. When temperature overshoot is detected, power supply was shut down immediately to prevent the tube failure, which enabled multiple CHF experiments on the same specimen. The temperature overshoot was determined by closely monitoring the temperature change respect to the time change (dT/dt = 25℃/s). Once preset dT/dt was detected, power supply was shut down.

Transient critical heat flux experiments were conducted on FeCrAl (C36M) alloy and Inconel600 tubes under atmospheric pressure. For FeCrAl alloy, transient CHF data was acquired to directly compare to the steady-state CHF data. For impartial comparison between steady-state CHF and transient CHF, flow condition and inlet equilibrium quality were set to that of the FeCrAl alloy's steady-state CHF point. It assumes thermodynamic quality at the instance of transient departure from nucleate boiling (DNB) does not change significantly [19]. By setting equilibrium quality equally, impartial comparison between steady-state CHF and transient CHF was made. For Inconel600 tubes, transient CHF experiments were carried out at a fixed inlet subcooling and various mass fluxes under atmospheric pressure to investigate effects of mass flux on transient CHF. For transient CHF experiments, a half sine shaped pulsed power with the pulse width of 1 second was applied. Pulsed width was designed to simulate a subprompt (<$1 of reactivity) hot full power reactivity initiated accident (RIA) in a light water reactor (LWR). Yet, it is still a much longer pulse width relative to a superprompt (>$1 of reactivity) [10,11]. Unlike steady-state CHF experiments, post-CHF flow boiling behaviors were analyzed with the measured voltage, current, and outer wall temperature as material did not fail due to CHF occurrence. Transient CHF was determined by

detailed analysis of boiling surface temperature change with respect to the heat flux change and time. Detailed procedure for transient CHF is presented in a later chapter.

Table 2.1. Flow boiling CHF experiment condition

	Pressure	Mass Flux	Inlet Subcooling	Input Power
Steady-state	84 kPa	200 ~ 2000 kg/m^2s	54,34, and 10℃	0.03 V increment at 30 – 40 s interval
Transient	84 kPa	200 ~ 600 kg/m^2s	10℃	Half sine shaped pulsed power, 1s width

In this study, experimentally measured CHFs are compared to the 2006 CHF lookup table predictions. In the city of Albuquerque, atmospheric pressure and boiling point are lower than the sea level due to high elevation. The lookup table predictions were converted to the Albuquerque atmospheric pressure for a fair comparison with the experimental data.

2.2.2 The Uncertainty Analysis

Transient CHF measurement uncertainty due to the thermocouple location is quantified with 5 K-type thermocouples with 0.005 mm diameter attached from the top end of the heated length at 5 mm intervals to the center of the test section. Transient CHFs attained from 5 different axial locations had a maximum difference of 3.3%.

Through both steady-state and transient CHF experiments, the fluid reservoir was open to the atmosphere at the identical water level to ensure a fixed pressure. The fluid temperature at the identical flow condition had less than ± 0.2℃ fluctuation from 13 cases. The measured flow velocity had less than $\pm 2\%$ uncertainties from 13 cases.

2.2 Tested Materials and Surface Characterization

2.3.1 Tested Materials

Steady-state flow boiling CHF experiments were performed on FeCrAl (C36M and C26M2), Inconel600, Monel400, SS304, SS316, Grade-2 Titanium, and Zircaloy-4 tubes. Same material with different thicknesses (Inconel600 and SS316) were used to investigate the implications of the heater thickness on the flow CHF. All the test specimen has an outer diameter of 9.525 mm with varying thicknesses. Prior to the experiments, the inner surface of the tubes was rinsed with acetone, methanol, and deionized water to remove any contamination. Transient flow boiling CHF experiments were performed on FeCrAl (C36M) and Inconel600 tubes. Table 2.2 shows the geometries of tested tube materials.

The alloy C36M is the first generation FeCrAl alloy and has a similar composition as the alloy C26M2, which is currently in the Hatch-1 commercial reactor for the test [32]. The autoclave corrosion testing of these two alloys shows behavioral indifference.

Table 2.2. Test tube geometries

Material	FeCrAl (C36M)	FeCrAl (C26M2)	Inconel600	Monel400	SS304	SS316	Grade 2 Titanium	Zircaloy-4
Inner Diameter (mm)	8.763	8.763	7.747 8.103 8.509	8.103	8.509	8.103 8.509 8.763	7.474	8.255
Thickness (mm)	0.381	0.381	0.889 0.711 0.508	0.711	0.508	0.711 0.508 0.381	0.889	0.635

2.3.2 Surface Wettability Measurement

A surface feature that is known to have a strong effect on CHF is the surface wettability. It is known that an increase in surface wettability enhances CHF [25]. In this study, the surface wettability of tested tube materials is measured following the procedure given by the American Society of Testing Materials (ASTM) [33]. The test tube was cut into half inch length. Then cut out pieces were axially divided into 3 pieces to analyze the surface morphology of the inner wall, where the boiling and CHF occurs.

The sessile drop technique was used to measure the static contact angle of a 5μL deionized water droplet on the inner surface of tube materials. Every measurement was taken in less than 30 seconds to prevent evaporation of droplet. The measurements were conducted at 20℃ room temperature at atmospheric pressure. Rame-Hart goniometer, as shown in Fig 2.4 is used to accurately control the droplet and to take photos of the contact angle of still droplets. Due to the curvature of the surface, contact angles of each droplet from the photos were manually measured using an on-screen protractor. To enhance

measurement reliability, multiple measurements were made on the same surface and average values are presented with standard deviations.

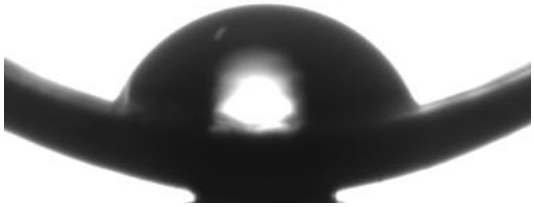

Figure 2.3 Contact angle measurement of SS316 (0.508mm) as-received inner surface

Figure 2.4 Rame-Hart goniometer model 590

2.3.3 Surface Roughness Measurement

Addition to the surface wettability, surface roughness is also known to have a strong effect on CHF as it is directly related to micro-cavities in the boiling surface,

which trigger bubble nucleation. Same tube coupons used in wettability measurements were used to measure surface roughness.

Veeco Dektak 150 surface profilometer, as shown in Fig 2.6, is used to measure hills and valleys of tube coupons. 2 mg force is applied on surfaces measuring 2000 µm length for the 30-second duration for accuracy enhancement. The scan rate was 0.222 µm/sample. Profilometer was controlled by a PC with built-in software to analyze the collected data, generating the average roughness, Ra, which is shown in Fig 2.5.

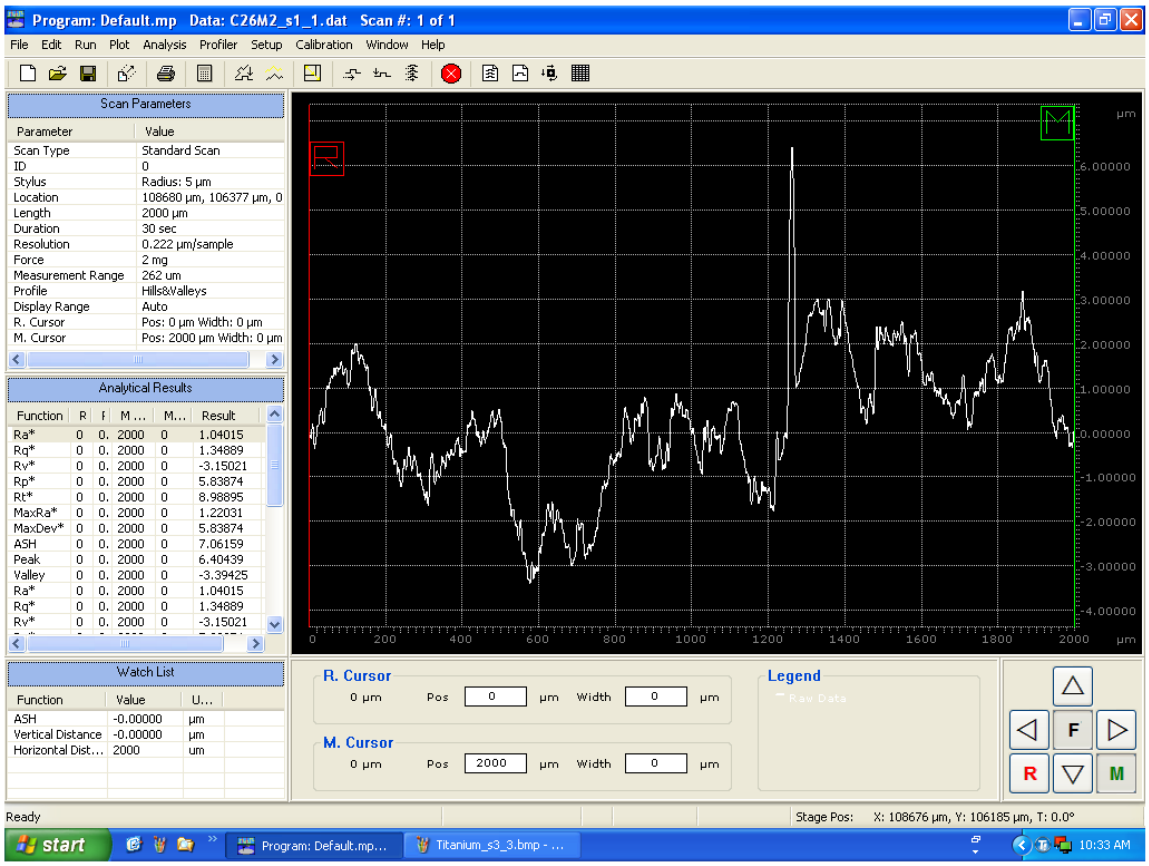

Figure 2.5 Surface roughness measurement of FeCrAl (C26M2) as-received inner surface

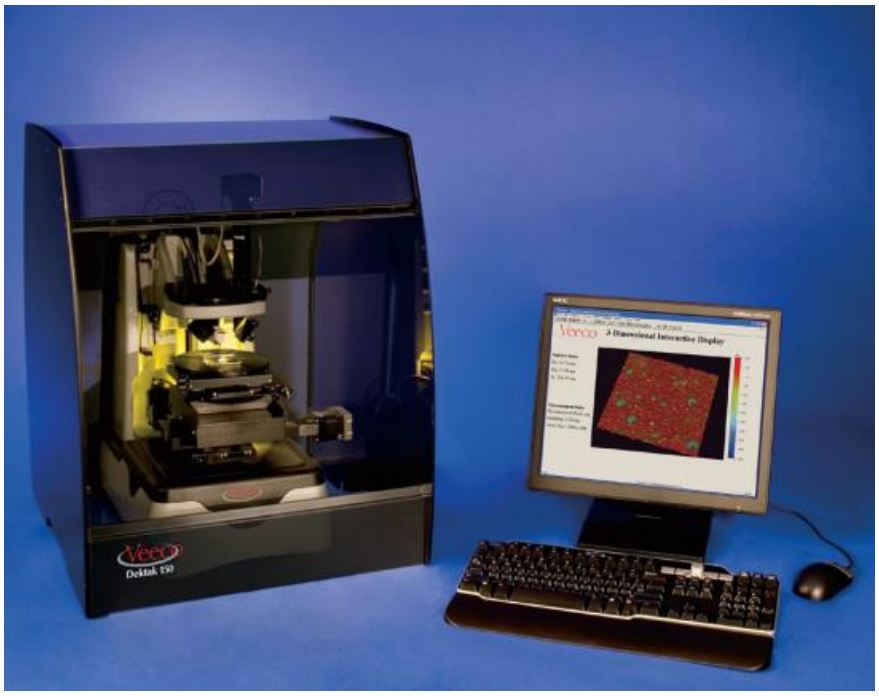

Figure 2.6 Veeco Dektak 150 profilometer

2.3.4 Scanning Electron Microscopy

Scanning electron microscopy (SEM) produces an image of a sample specimen by focusing an electron beam across the surface. Secondary electrons emitted by atoms on the surface excited by the electron beam are detected in a high vacuum chamber, generating light contrast variation images.

The Thermo Scientific Quanta 3D FEG and JEOL JSM-IT100 scanning electron microscopes are used to generate SEM images of the test specimen inner surfaces, where actual boiling occurs. Microscopes were controlled by a PC with built-in software to analyze the collected data. In this study, SEM images were taken to investigate surface morphology differences and to confirm the evolution of the oxide layer.

2.3.5 Atomic Force Microscopy

Atomic force microscopy (AFM) produces high-resolution topography of a sample specimen by measuring the force reaction of the probe to the imposed sample specimen.

Witec Alpha 300 atomic force microscope is used to generate AFM topography of FeCrAl samples' inner surfaces (fresh, 500 hour and 1000 hour oxidized). For AFM measurement, the non-contact alternating current mode is utilized across the area of 5 microns by 5 microns at a scan speed of 0.5 s/line. The microscope was controlled by a PC with built-in software to analyze the collected data to produce roughness parameters. AFM topography was taken to confirm oxidation growth on oxidized FeCrAl samples.

Chapter 2 Nomenclature

$L_{entrance}$	Entrance length
D_{tube}	Inner diameter of test tube
Re	Reynolds number
u	Velocity of the fluid
D_h	Hydraulic diameter
v	Kinematic viscosity

CHAPTER 3. SUBCOOLED STEADY-STATE CHF STUDY

3.1 Steady-state CHF Results for FeCrAl, Zircaloy, and Inconel

I have published results in this chapter in [39]. In this chapter, steady-state CHF experiments were performed at a fixed flow condition (300 kg/m^2s) under atmospheric pressure with a fixed inlet subcooling (54℃ and 34℃) on FeCrAl (C36M), Inconel600, and Zircaloy-4 tubes. Multiple CHF experiments were conducted on the same tube surface to analyze the effect of surface morphology change on flow boiling CHF.

Flow CHFs were measured by quantifying the measured voltage and current into heat flux at the temperature overshoot:

$$q''_{CHF} = \frac{Power}{Area_{heated}} = \frac{\Delta V \cdot I}{\pi \cdot D \cdot L} \tag{3.1}$$

Equilibrium quality of each attained data was used to make a direct comparison to the 2006 Groeneveld lookup table. Equilibrium quality (X_e) was calculated at the location of CHF(z_{CHF}) using energy balance in the axial direction of the heated length:

$$X_e(z_{CHF}) = \frac{h_m^+(z_{CHF}) - h_f}{h_{fg}} \tag{3.2}$$

$$h_m^+(z_{CHF}) = h_{in} + \frac{1}{\dot{m}} \int_0^{z_{CHF}} q' \, dz \tag{3.3}$$

With the above equations, the experimental CHF values for each tube materials are evaluated and presented in Fig 3.1. Total 13 points of repeated CHF data are shown for each tested tube materials with an average value and the lookup table prediction at the corresponding equilibrium quality. CHF data from FeCrAl and Inconel600 tubes were collected at a 54℃ inlet subcooling. The Zircaloy-4 data were collected from two inlet

subcoolings (54℃ and 34℃); thus, two average values are presented with two lookup table predictions at corresponding equilibrium qualities. Numbers written in Fig 3.1 (a) – (c) represent the average CHF values with standard deviations, which are less than 10 % of its average CHF values. It is notable that measured CHF does not change significantly with repeated experiments. Presented average CHF values showed that FeCrAl alloy has 22% and 14% higher value compared to Zircaloy-4 and Inconel600, respectively. Throughout the repeated experiments, the nucleate boiling heat transfer coefficients were measured, which showed increasing fluctuation with repeated experiments. It implies that the surface morphology change (i.e., oxide layer formation) may have limited significance on CHF under the tested flow condition.

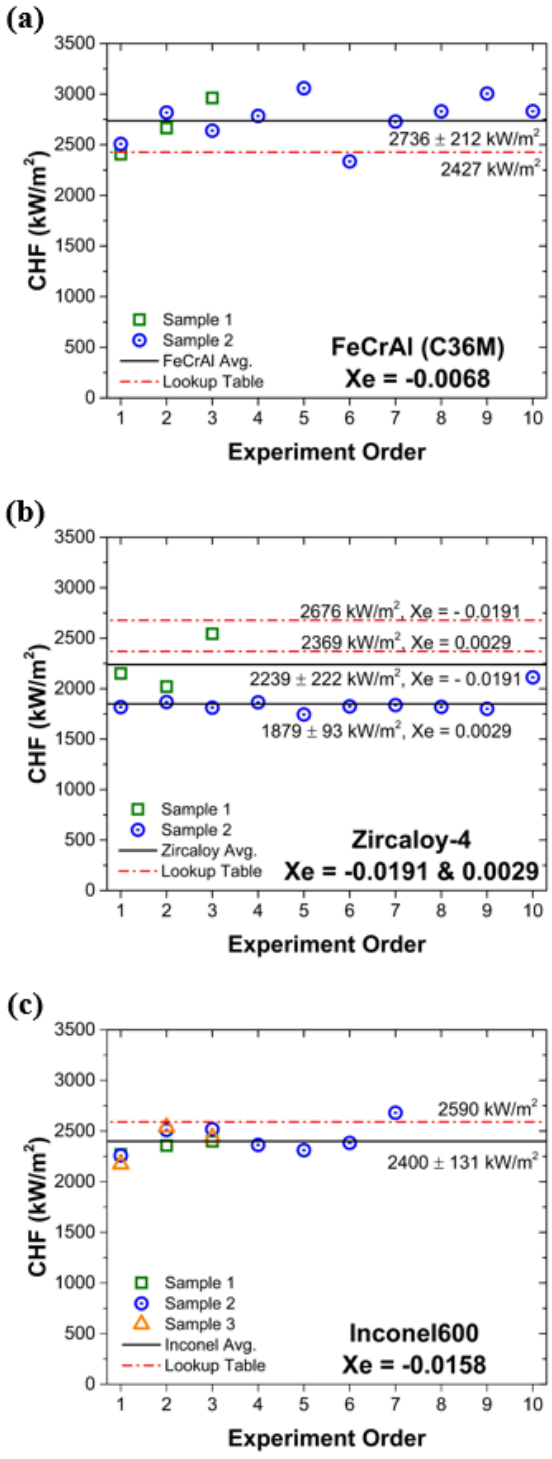

Figure 3.1 Multiple CHF measurements on the same tube surface (a) FeCrAl (C36M) alloy, (b) Zircaloy-4, and (c) Inconel600 tubes. (54℃ and 34℃ inlet subcooling, 84 kPa, and 300 kg/m^2s)

Fig 3.2 presents the average measured CHF data of three tube materials compared to the lookup table prediction at the corresponding equilibrium qualities. Inconel600 CHF data has -7% percent error compared to the lookup table prediction, showing relatively good agreement. Zircaloy-4 CHF data shows -16% and -22% decreased values compared to the lookup table predictions. FeCrAl alloy CHF data shows 13% increased value relative to the lookup table prediction, suggesting an increased departure of nucleate boiling ratio (DNBR) margin compared to the Zircaloy and Inconel tubes.

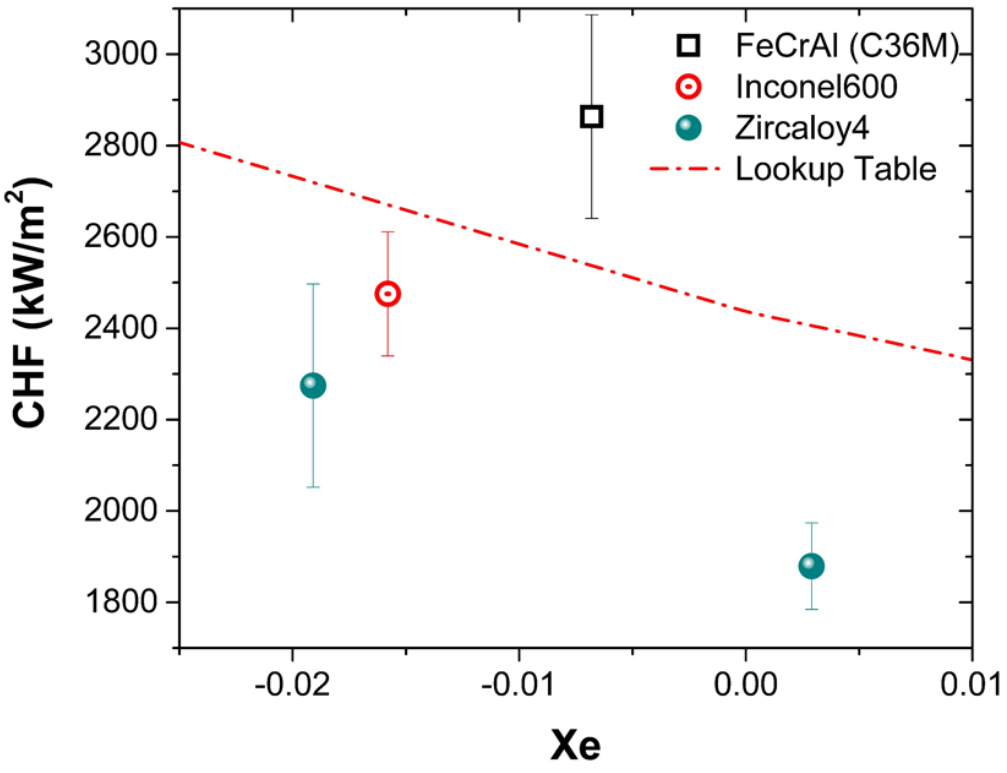

Figure 3.2 Measured CHF data of FeCrAl alloy, Zircaloy-4, and Inconel600 tubes compared to the 2006 Groeneveld lookup table prediction as the corresponding equilibrium quality

3.1.1 Effect of Surface Morphology on CHF

Surface wettability and roughness are known to have a strong effect on CHF. An increased surface wettability enhances CHF as it promotes rewetting of dry patches, which are developed on the boiling surface due to evaporation. Surface roughness is known for its direct association with the micro-cavities, which may act as bubble nucleation sites in the boiling surface. An increased surface roughness implies an increased number of bubble nucleation sites, which enhances nucleate boiling heat transfer and CHF. In this study, surface wettability and roughness of as-received and post-CHF surfaces were measured and compared to investigate its implication on CHF.

For post-CHF measurements, sample number 2 of each material shown in Fig 3.1 (a)-(c) were used. As shown in Fig 3.3, five measurements were made on each surface and average values were used for comparison. Measurements of post-CHF surfaces show increased wettability relative to as-received surfaces for all materials. The oxidation layer growth on the boiling surface was expected by running multiple boiling CHF experiments. Even with rapid shut down of the power supply at the temperature overshoot, boiling surface reached several hundred degrees for the oxide layer to grow. Hence, oxide layer formation is considered responsible for the changes in surface characteristics. Measured contact angle differences of as-received and post-CHF surfaces are 15.79°, 12.44°, and 17.87° for FeCrAl alloy, Zircaloy-4, and Inconel 600 respectively. An appreciable change in wettability can be seen in the range of 50° to 80°; yet, no significant change in CHF was observed for tested tube materials. This result implies that surface wettability change in the range of 50° to 80° has restricted impact on

flow CHF. Yet, extreme surfaces (i.e., super-hydrophobic or super-hydrophilic surfaces) may still have an impact on flow CHF.

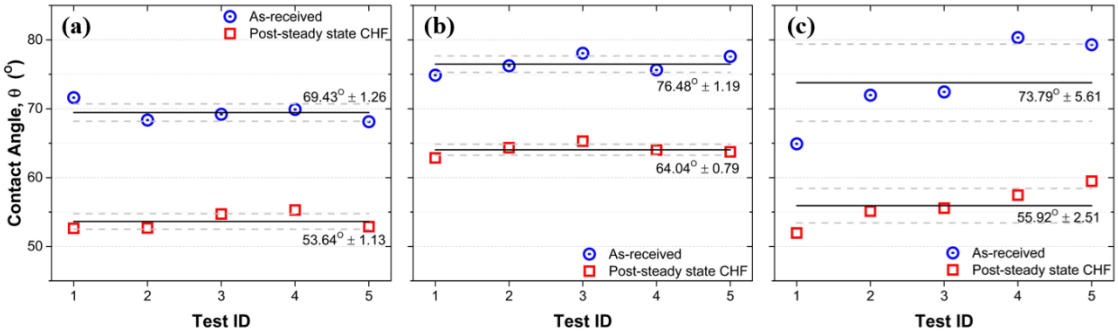

Figure 3.3 Surface wettability comparison of as-received and post-CHF surfaces for (a) FeCrAl (C36M) (10 CHF experiments, (b) Zircaloy-4 (10 CHF experiments), and (c) Inconel 600 (7 CHF experiments), the dashed lines indicate standard deviations

Measured surface roughness differences of as-received and post-CHF surfaces are 4.10 μm, 2.89 μm, and 0.81 μm for FeCrAl alloy, Zircaloy-4, and Inconel 600 respectively. Similar to the surface wettability analysis, appreciable changes in surface roughness are observed as shown in Fig 3.4. In spite of a notable change in surface roughness by 4 μm, CHFs of tested materials rather stayed unchanged in the repeating experiments. It implies insignificance of surface roughness on flow boiling CHF.

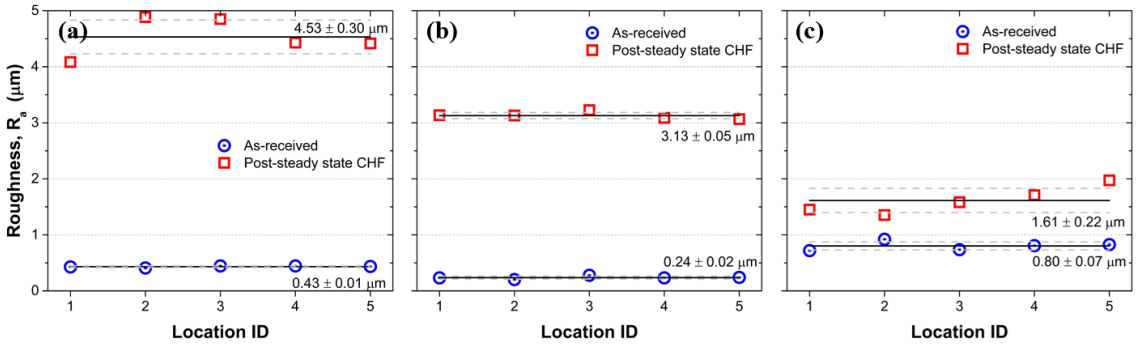

Figure 3.4 Surface roughness comparison of as-received and post-CHF surfaces for (a) FeCrAl (C36M) (10 CHF experiments, (b) Zircaloy-4 (10 CHF experiments), and (c) Inconel 600 (7 CHF experiments), the dashed lines indicate standard deviations

To ensure a change in surface morphology, scanning electron microscopy (SEM) images were taken after the surface wettability and roughness measurements, as shown in Fig. 3.5 – 3.7. The SEM image of FeCrAl alloy shows rather densely formed oxide layer with dislocations (Fig 3.5 (b)). The SEM image of Zircaloy-4 and Inconel600 surfaces show homogeneously formed oxide layer compared to that of FeCrAl alloy (Fig 3.6 (b) and Fig 3.7 (b)). This concludes that oxide layer formation changed surface wettability and roughness by 12° to 18° and by 1 μm to 4 μm; yet, the experimental results show no significant change in CHF.

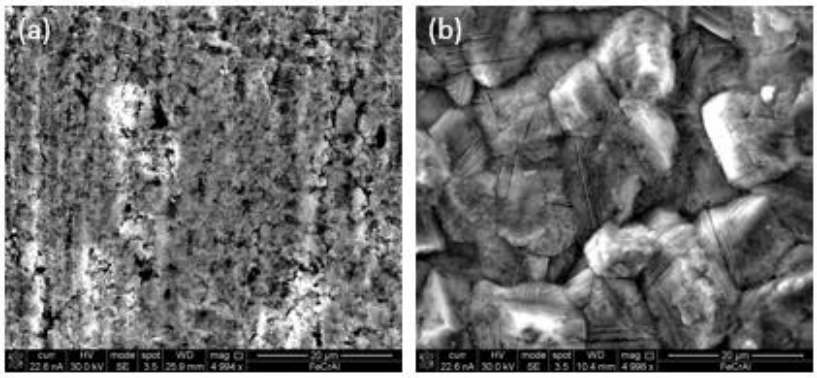

Figure 3.5 SEM micrograph of FeCrAl (C36M) alloys inner surface in (a) as-received, (b) after 10 steady-state CHF measurements

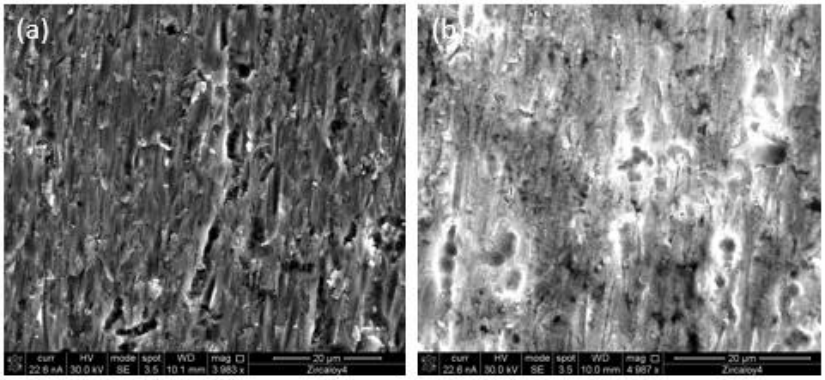

Figure 3.6 SEM micrograph of Zircaloy-4 inner surface in (a) as-received, (b) after 10 steady-state CHF measurements

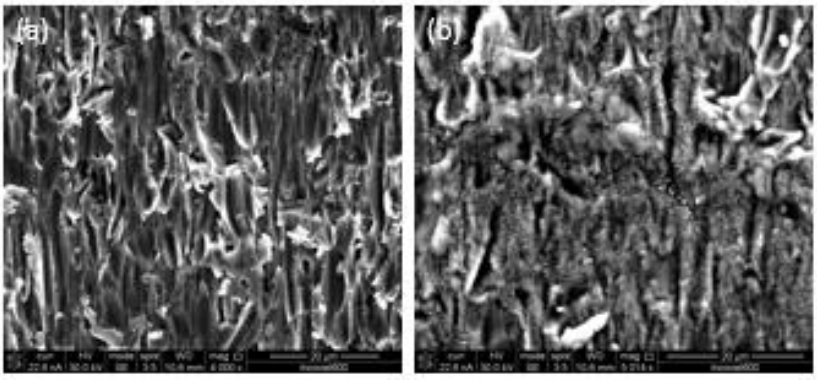

Figure 3.7 SEM micrograph of Inconel 600 inner surface in (a) as-received, (b) after 7 steady-state CHF measurements

3.1.2 Effect of Thermal Parameter on CHF

With observed insignificance of surface characteristics on flow boiling CHF, thermal parameters were investigated to explain apparent CHF differences among the tested tube materials.

Thermal effusivity, $e = \sqrt{k \cdot \rho \cdot c_p}$, is a measure of the material ability to exchange thermal energy with surroundings. A material exhibiting higher thermal effusivity is likely to have a higher influence in thermal energy exchange with its surrounding in transient conduction. An analytical solution for the prompt interface temperature upon the contact of two infinite media (Eq 3.4) can help explaining the effect of thermal effusivity [34].

$$T_{interface} = \frac{\left(\sqrt{k \cdot \rho \cdot c_p}\right)_A \cdot T_A + \left(\sqrt{k \cdot \rho \cdot c_p}\right)_B \cdot T_B}{\left(\sqrt{k \cdot \rho \cdot c_p}\right)_A + \left(\sqrt{k \cdot \rho \cdot c_p}\right)_B} \quad (3.4)$$

As implied by Eq 3.4, the media with a higher thermal effusivity has more significance in the interface temperature. In the boiling process, the media with a higher thermal effusivity exhibits a higher interface temperature upon the quenching of cold water. Hence, thermal effusivity of material regulates the interface temperature, which directly impacts the thermal gradient of the liquid micro-layer on the heated surface. The thermal gradient of the liquid micro-layer controls the size of bubble nucleation; hence, controls the number of nucleation sites on the heating surface. A material with higher thermal effusivity enlarges the number of active nucleation sites, promoting more effective heat transfer from a solid to the contacting fluid. It may prevent irreversible dry spot formation and enhance CHF as a consequence. [35]

A thermal activity can be explained as an extension of the thermal effusivity. The solid conduction in a heating element has a finite length scale for the mass, energy, and

momentum transfer. The boiling process in a solid–liquid interface also exhibits a finite time scale. Unless a solid is sufficiently thick enough, the finiteness of material size is likely to impact the boiling heat transfer. To account the finiteness of the heat transfer media, material wall thickness (δ) is accounted with thermal effusivity, $\delta\sqrt{k \cdot \rho \cdot c_p}$. Pool boiling studies investigated its relation to CHF, which showed an asymptotical increase in pool CHF relative to material wall thickness increase until it reaches a sufficient thickness where the heater thickness does not play a role in the boiling heat transfer [35-38].

Thermal diffusivity, $\alpha = \frac{K}{\rho \cdot C_p}$, is a parameter governing the rate of temperature change in transience. High thermal diffusivity promotes heat flow into the local cold spot in a solid media, thereby enhancing fast recovery of the surface temperature in the boiling process. Theoretically, Thermal diffusivity is considered inversely proportional to CHF.

Surface thermal economy, $\frac{(\rho \cdot C_p)^{3/2}}{\sqrt{k}}$, is another thermal parameter developed by Lee et al [39]. Two contrary parameters, thermal effusivity and thermal diffusivity are accounted together to quantify the ratio of the material ability to transfer heat to the contacting liquid to the material ability to avoid the formation of irreversible dry spots in solid. These two competing effects are shown in Fig 3.8.

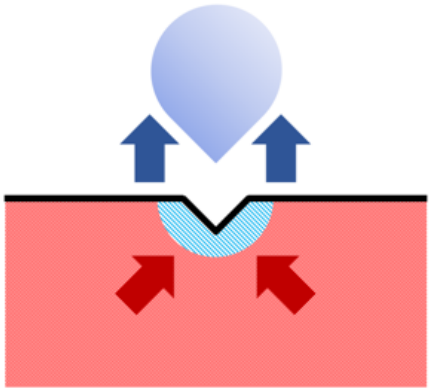

Heat dissipation to contacting liquid $\sim\sqrt{k\rho c_p}$

Cold spot recovery transition in solid $\sim k/\rho c_p$

Figure 3.8 Two competing material thermal parameters governing the interface temperature change rate of the boiling surface

Above four thermal parameters are plotted relative to the measured CHF values in Fig 3.8. No clear trends were observed from thermal effusivity and thermal activity. While thermal diffusivity and surface thermal economy parameters showed a clear trend for the tested materials to a certain degree, given range of the parameters may be limited by the tested materials; thereby, a wider range of materials needed to be investigated.

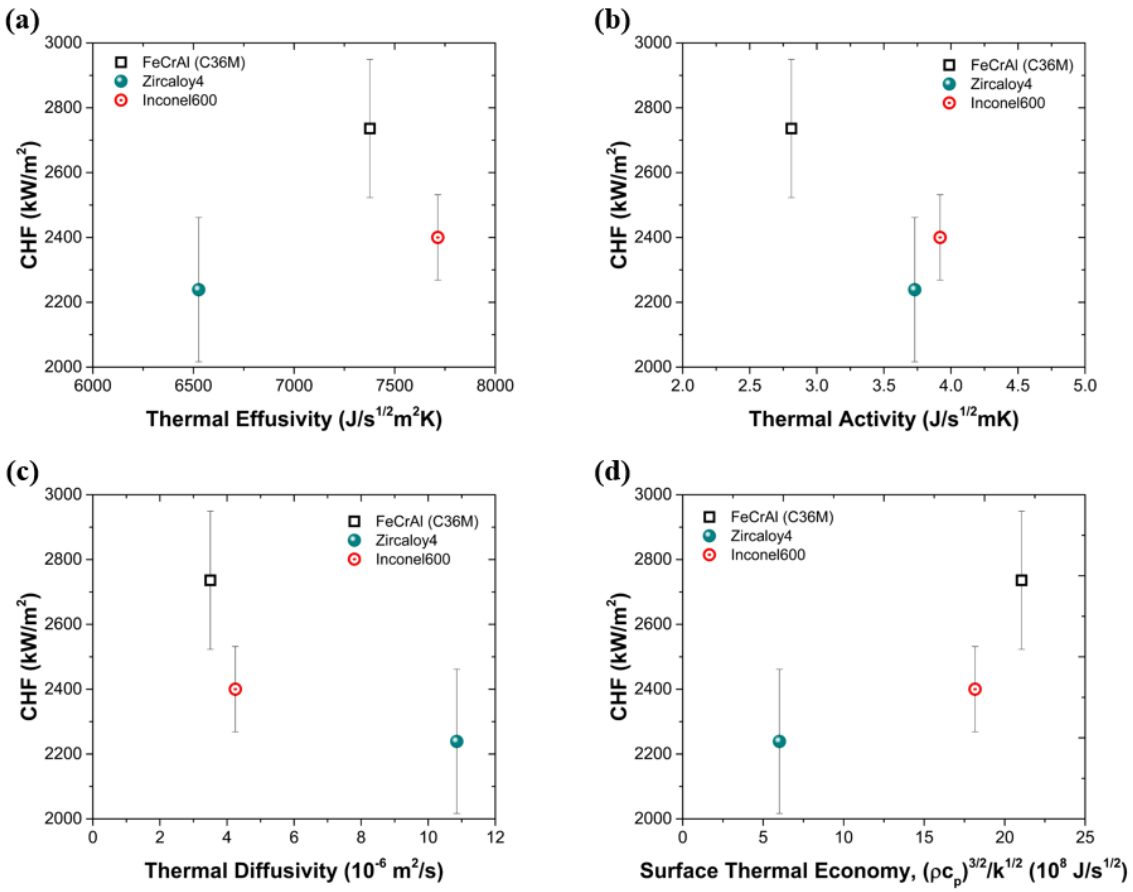

Figure 3.9 Measured CHF relative to (a)Thermal effusivity, (b)thermal activity, (c)thermal diffusivity, and (d)surface thermal economy

Chapter 3 Nomenclature

q''_{CHF}	Critical Heat Flux
ΔV	Voltage drop across the heated length at the temperature overshoot
I	Current at the temperature overshoot
D	Inner diameter of the test tube
L	Heated length of the test tube
X_e	Equilibrium quality
h_m^+	Mixed enthalpy obtained using energy balance
h_f	Saturated liquid enthalpy
h_{fg}	Enthalpy of vaporization
h_{in}	Inlet enthalpy
$\dot{m}$	Mass flow rate
q'	Linear heat rate applied in the heated length
z_{CHF}	Location of CHF
k	Thermal conductivity
ρ	Density
c_p	Specific heat
T	Temperature
δ	Material thickness
α	Thermal diffusivity

CHAPTER 4. STATISTICAL STEADY-STATE CHF STUDY

4.1 Statistical Steady-state CHF Results

I have submitted results in this chapter for journal publication. It is under review [40,42]. In this chapter, a wide range of materials were considered to investigate implications of surface characteristics, thermal parameters, and mass flux on flow boiling CHF. Same material with varying thicknesses was utilized to investigate implications of the heater thickness on the flow boiling CHF. Experiments were performed under varying flow condition from 200 kg/m^2s to 2000 kg/m^2s at atmospheric pressure with fixed 10℃ inlet subcooling. Flow CHFs were quantified using the same method described in chapter 3.

Table 4.1 shows a number of tubes used to acquire a number of CHF data at each mass flux for each material tested. Up to 800 kg/m^2s mass flux, most test specimens did not fail from the CHF occurrence due to relatively low heat flux, which enabled to run multiple experiments on the same tube. Above 800 kg/m^2s, test tubes failed even with rapid shut down of the power supply. Selected mass fluxes for each material varies due to limited applicable power from the power supply. As tubes were heated by Joule heating, materials with a higher electrical resistivity induce higher voltage drop across the given heated length.

Table 4.1 Steady-state CHF experiment matrix

	Mass Flux (kg/m^2s)	200	400	600	700	800	900	1000	1200	1400	1500	1600	2000
FeCrAL(0.381mm)	# of tube tested	1						1			1		1
	# of CHF acquired	3						1			1		1
Inconel600(0.508mm)	# of tube tested	1	1	1		1		3	3	3	3		
	# of CHF acquired	3	3	3		3		3	3	3	3		
Inconel600(0.711mm)	# of tube tested	1	1	1									
	# of CHF acquired	3	3	3									
Inconel600(0.889mm)	# of tube tested	1	1										
	# of CHF acquired	3	3										
Monel400(0.711mm)	# of tube tested	1											
	# of CHF acquired	3											
SS304(0.508mm)	# of tube tested	1	2	1									
	# of CHF acquired	3	3	3									
SS316(0.381mm)	# of tube tested	1	1	2		2		3	1	1		1	
	# of CHF acquired	3	3	3		3		3	1	1		1	
SS316(0.508mm)	# of tube tested	1	1	1		1		1	1				
	# of CHF acquired	3	3	2		2		1	1				
SS316(0.711mm)	# of tube tested	1											
	# of CHF acquired	3											
Titanium(0.889mm)	# of tube tested	1											
	# of CHF acquired	3											
Zircaloy-4(0.635mm)	# of tube tested	1	1	1	2	2	1						
	# of CHF acquired	3	2	3	3	3	1						

Steady-state CHF occurred at different applied heat fluxes for the tested materials, resulting in varying equilibrium qualities. Later in this chapter, measured CHFs are compared to the 2006 Groeneveld lookup table predictions at the corresponding equilibrium qualities to show its variance among tested materials and against tested mass fluxes.

Fig 4.1 shows the measured CHFs for 11 tube materials. Fig 4.1(a) shows the measured CHFs from as-machined fresh tube surfaces and Fig 4.1(b) shows the average of measured CHFs with standard deviation shown as error bars. The maximum and minimum standard deviation of CHFs for all tested materials are 14% (SS316 (0.711mm) at 200 kg/m^2s) and 1% (FeCrAl (C26M2, 0.381mm) at 200 kg/m^2s) with average of 4% from 34 CHF values. Measured standard deviations of attained CHF values are very low, representing the credibility and consistency of the experimental results. CHF values of different materials tend to converge with increasing mass flux. CHF values from the

average data converge more relative to the fresh data due to the normalized error of CHF nature.

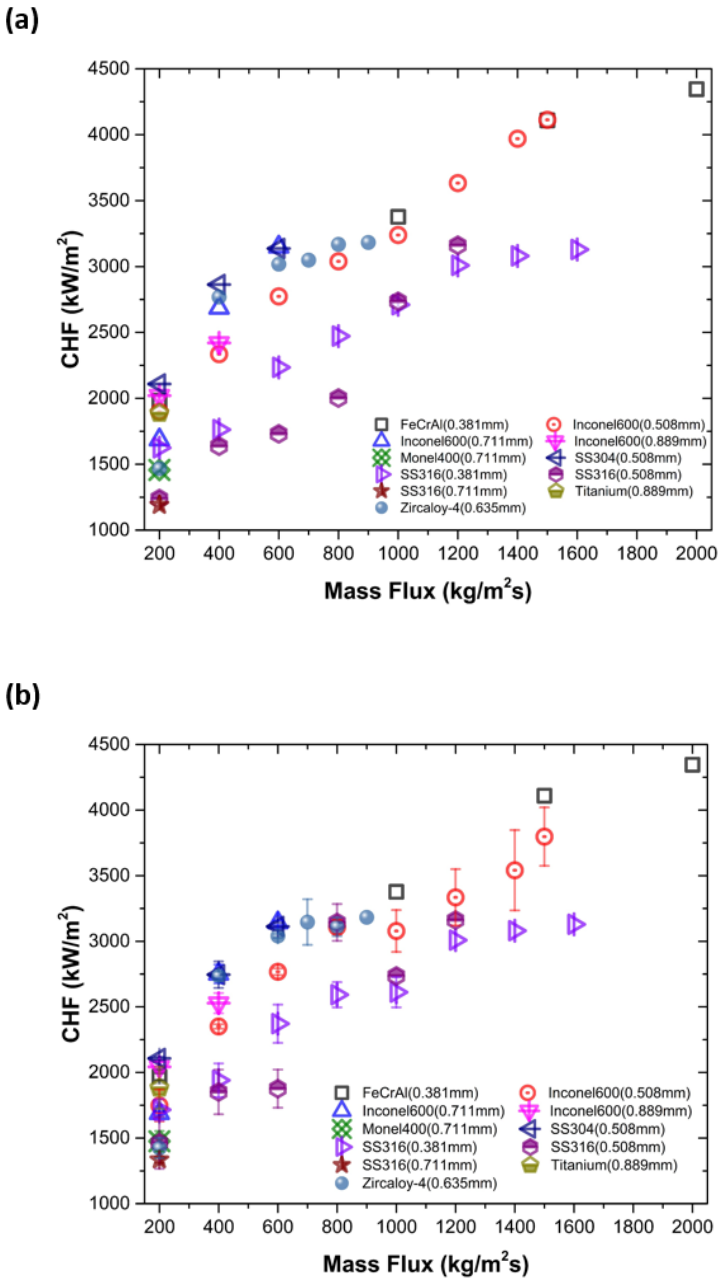

Figure 4.1 Steady-state CHFs of tube materials: (a) fresh tube data (b) average data (200 kg/m^{2}s - 2000 kg/m^{2}s mass fluxes, 10°C inlet subcooling, 84kPa atmospheric pressure)

4.1.1 Effect of Mass Flux on CHF

While an increase in mass flux increases CHF, it is unknown what causes apparent CHF differences among different materials under tested flow condition. In this study, the statistical approach accounting CHF variation from different materials is made to investigate the effects of mass flow on CHF. Measured CHFs were compared to each other using the absolute percent differences:

$$\text{Absolute Percent Difference} = \frac{|CHF_A - CHF_B|}{\left(\frac{CHF_A + CHF_B}{2}\right)} \times 100 \quad (4.1)$$

Calculated absolute percent difference values were averaged at the corresponding mass flux as shown in Fig 4.2. As mass flux 200 $\mathrm{kg/m^2 s}$, 11 CHF values were acquired from 11 materials. These 11 CHF values were compared to each other, resulting in 55 different absolute percent difference values. Average of 55 absolute percent difference values are fitted in Fig 4.2. A number of tested materials vary with increasing mass flux due to the limitation of applicable heat flux from the power supply. Increase in mass flux decreases apparent CHF gaps among tested materials under the tested condition. This result indicates that an increase in mass flux may diminish other implications on CHF like surface morphology or material thermal properties.

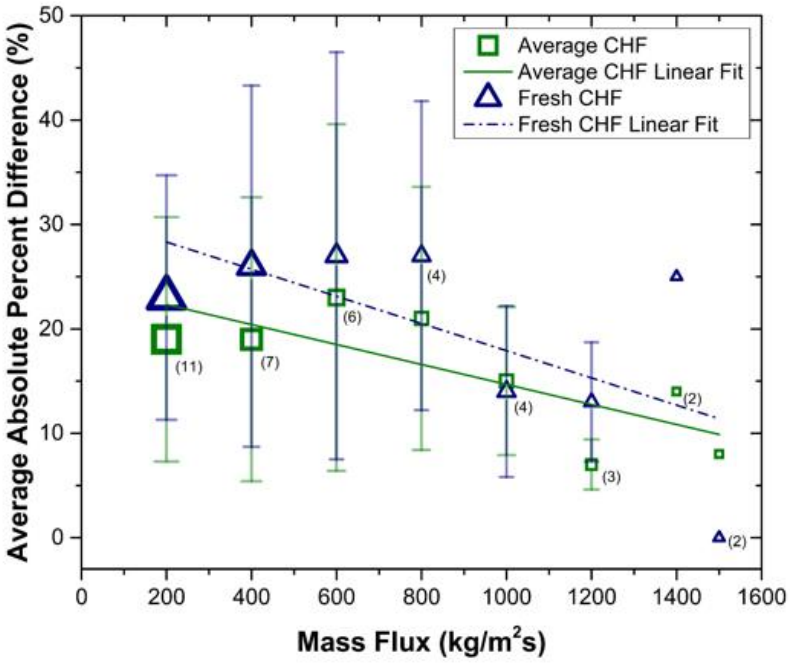

Fig 4.2 Average absolute percent difference of measured CHFs among tested tube materials for fresh and average data (size of data point and numbers in parentheses indicate number of tested materials)

While Fig 4.2 shows convincing trends, not all materials are weighted equally along tested flow conditions. Hence, investigation through every possible range of mass flux was conducted to avoid impartial comparison from not having the same number of the test specimen. In Fig 4.3, the average absolute percent difference of 21 different ranges of mass fluxes are shown with linear fits. For CHFs of fresh tubes, 12 out of 21 ranges have a negative slope indicating CHF gaps among tested materials decrease with increase in mass flux. While the average absolute percent difference from 9 ranges shown to have positive trends, it does not necessarily specify increased CHF gaps among tested materials. Increase in absolute CHF value at a higher mass flux naturally leads to

increased error in acquired CHF value. Considering that increased error of acquired CHF at higher mass flux, slightly positive slope in average absolute percent difference does not necessarily mean an increase in CHF gaps due to mass flux. Similar trends are observed in Fig 4.3(b) for average CHF data, which shows 14 out of 21 ranges have negative slopes, thereby representing a decrease in CHF gaps among different materials with an increase in mass flux.

(a)

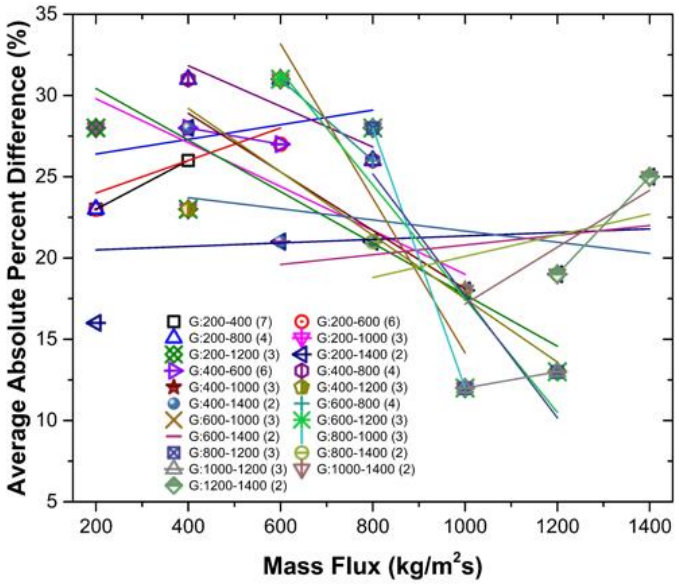

(b)

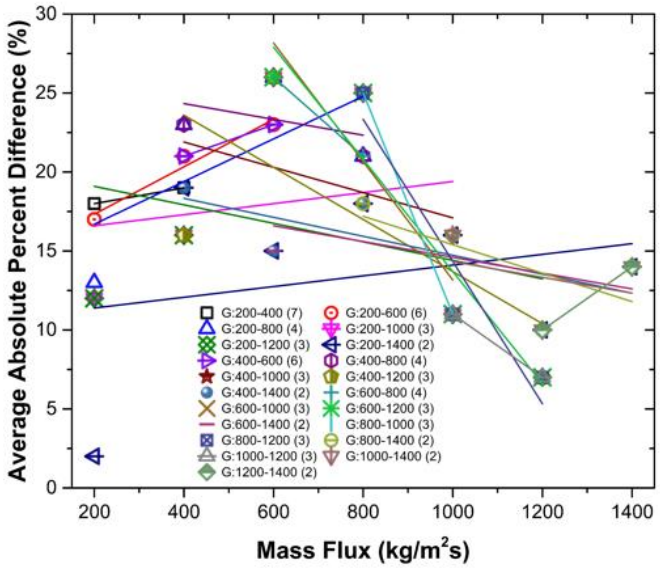

Fig 4.3 Average absolute percent difference of various tested mass flux ranges having same number of test specimen: (a) fresh tube data (b) average data (numbers in legend indicate number of tested materials in the corresponding range)

4.1.2 Statistical Comparison of CHF Data to Lookup Table Prediction

Above Fig 4.2 and 4.3 show dominant decreasing trends in average absolute percent difference of measured CHFs among tested tube materials. Yet, these two comparisons have no frame of reference as only experimental data were used. Therefore, a comparison between experimental data and the CHF lookup table predictions are made at the corresponding equilibrium quality or critical quality.

Table 4.2 shows the absolute percent difference of measured CHFs compared to the lookup table predictions at the corresponding equilibrium qualities for fresh tube data and average data. While experimental data of SS316 (0.381mm) show good agreement with the lookup table predictions, CHFs of other materials show relative differences.

Table 4.2 Measured CHFs compared to the CHF lookup table predictions

	Mass Flux (kg/m^2s)		200	400	600	700	800	900	1000	1200	1400	1500	1600	2000
FeCrAl(0.381mm)	Fresh	%	28						21			23		18
	Average		28						21			23		18
Inconel600(0.508mm)	Fresh		23	15	20		20		15	23	22	22		
	Average		12	16	20		23		10	14	9	13		
Inconel600(0.711mm)	Fresh		7	33	35									
	Average		6	35	35									
Inconel600(0.889mm)	Fresh		31	19										
	Average		32	24										
Monel400(0.711mm)	Fresh		12											
	Average		9											
SS304(0.508mm)	Fresh		37	41	36									
	Average		37	37	35									
SS316(0.381mm)	Fresh		4	20	5		2		3	4	4		6	
	Average		10	8	2		3		7	4	4		6	
SS316(0.508mm)	Fresh		32	30	35		27		3	8				
	Average		10	15	26		19		3	8				
SS316(0.711mm)	Fresh		40											
	Average		23											
Titanium(0.889mm)	Fresh		21											
	Average		21											
Zircaloy-4(0.635mm)	Fresh		11	37	30	30	25	24	18					
	Average		15	35	31	31	29	22	18					

Fig 4.4 shows the plot of the table with the linear fits for each material. It can be inferred that for most of the tested materials increase in mass flux closes the gap between measured CHFs to the lookup table predictions. For the average data, all the materials

show decreasing trends except for Inconel600 (0.711mm), which indicates material effect diminishes with increasing mass flow. It is notable that gaps between CHF and the lookup table predictions are decreasing even with increased CHF at a higher mass flux under the tested condition. It suggests that under extremely high mass flow rate, CHFs of different materials may converge sharply with the domination of the flow effect.

(a)

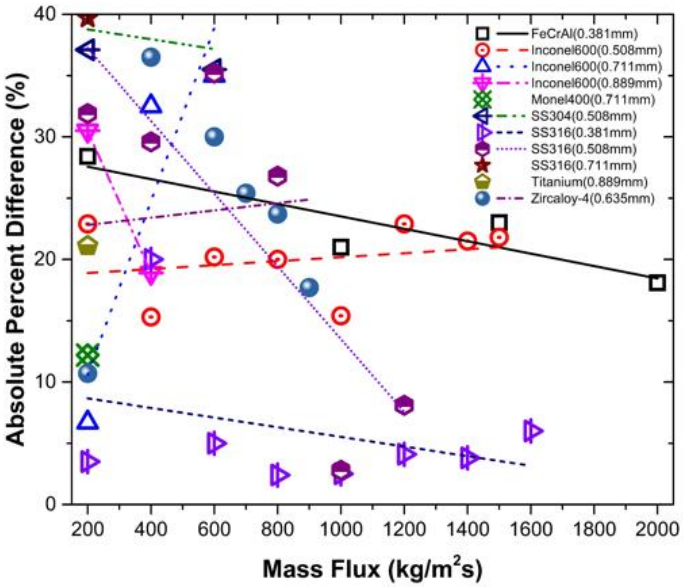

(b)

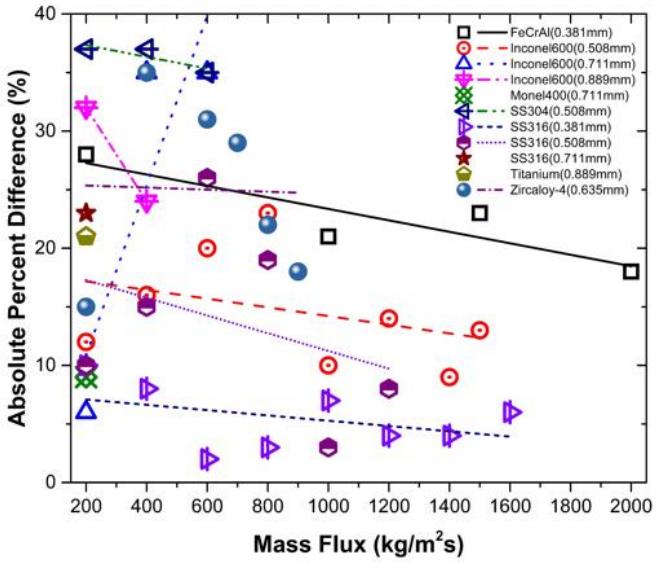

Figure 4.4 Absolute percent difference of measured CHFs to the lookup table predictions at the corresponding equilibrium qualities as a function of mass flux: (a) fresh tube data (b) average data

Fig 4.5 shows the average absolute percent difference of measured CHFs to the lookup table predictions relative to mass flux. It shows overall similar trends to Fig 4.5 indicating reducing gaps between CHFs and the lookup table predictions with increasing mass flux.

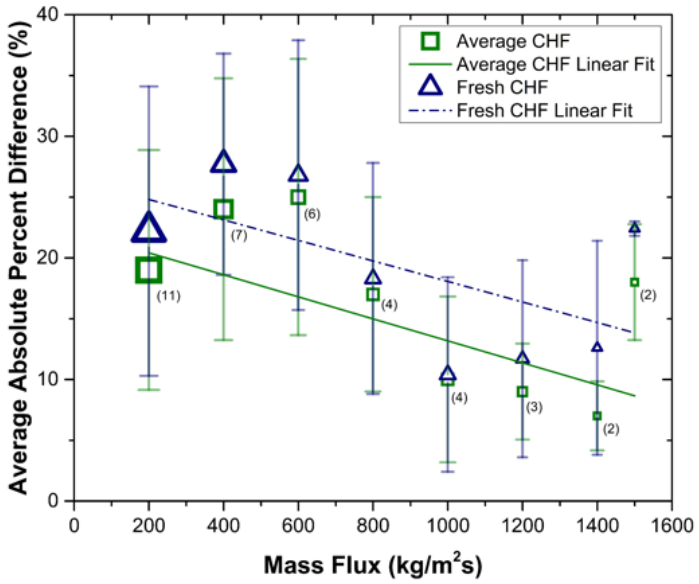

Figure 4.5 Average absolute percent difference of measured CHFs among tested tube materials to the lookup table predictions at the corresponding equilibrium qualities as a function of mass flux (size of data point and numbers in parentheses indicate number of tested materials)

From this analysis, it can be concluded that effect of high mass flux may diminish other effects (i.e., surface characteristics and material thermal parameters) on flow boiling CHF, under the tested materials and flow conditions.

4.1.3 Effect of Heater Thickness on CHF

Pool boiling studies revealed the effect of the heater thickness on CHF [35-38]. An increase in the heater thickness asymptotically enhances CHF up to the limiting value, where the thickness does not play a role. To examine the heater thickness effect under the flow condition, the same material with an increasing thickness (Inconel600: 0.508mm to 0.889mm, SS316: 0.381mm to 0.711mm) were used to conduct CHF experiments. In Fig 4.6, average CHF values with standard deviation shown as error bars are plotted. For SS316, unlike pool boiling studies, measured CHF decreased with increase in the heater thickness for all three flow conditions. Inconel600 showed a similar trend with SS316 under 200 kg/m^2s between the thickness 0.508mm and 0.711mm. Yet, beyond 200 kg/m^2s mass flux, CHF increased with increase in the heater thickness.

Contrary to the heater thickness studies in pool boiling, measured flow CHFs showed inconsistency relative to the heater thickness. SS316 showed consistently decreasing trend with increasing thickness for all three flow condition; but, Inconel600 showed inconsistency relative to both heater thickness and flow conditions.

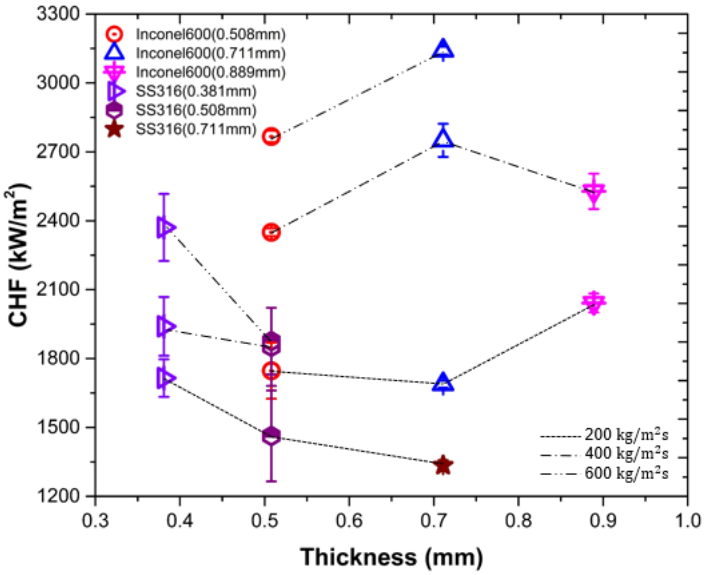

Figure 4.6 Measured CHFs of Inconel600 and SS316 as a function of the heater thickness under different mass fluxes

4.2 Steady-state Boiling Heat Transfer Results

In this section, above tested materials' boiling behavior from the single phase convection to nucleate boiling to CHF are analyzed. To compare the boiling behavior of tested materials, experimental results from 200 kg/m^2s to 1500 kg/m^2s are utilized to construct boiling curves. Presented data in this section for constructing boiling curves utilized experimental data on fresh tubes with fresh thermocouples to avoid any possible damage from the CHF occurrence.

Boiling curves in this section are obtained using measured heat flux and calculated inner wall surface temperature using 1-D steady-state heat conduction equation:

$$q'' = -k\frac{dT}{dr} \tag{4.2}$$

Fig 4.7 shows boiling curves of tested tube materials at various mass flux from 200 kg/m^2s to 1500 kg/m^2s, which curves are obtained with the steady-state experimental data up to the CHF points. It is notable that with increasing mass flux boiling curves of different materials consolidate into one similar shape in both single phase convection and nucleate boiling regimes. This result suggests that the effect of surface properties and/or material properties may play a significant role under the relatively low mass flow condition. Yet, under the relatively high mass flow condition, the effect of mass flux may dominate other implications that affect boiling heat transfer in tested materials and flow conditions.

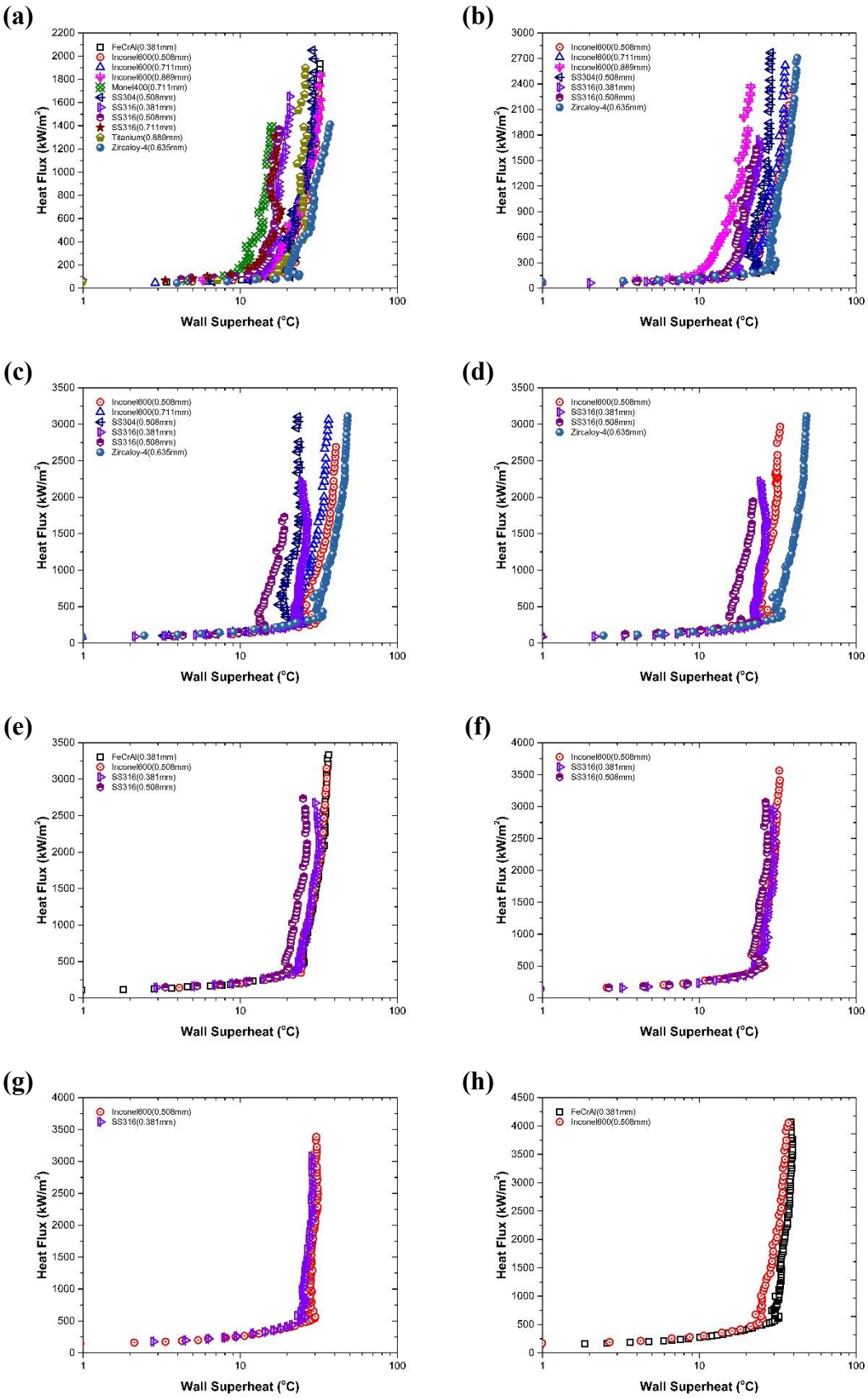

Figure 4.7 Flow boiling curves of tested tube materials at mass flux (a) 200 kg/m^2s, (b) 400 kg/m^2s, (c) 600 kg/m^2s, (d) 800 kg/m^2s, (e) 1000 kg/m^2s, (f) 1200 kg/m^2s, (g) 1400 kg/m^2s, and (h) 1500 kg/m^2s (85kPa, 10℃ inlet subcooling)

4.2.1 Effect of Mass Flow on Boiling Heat Transfer Coefficient

Fig 4.8 shows the boiling heat transfer coefficient of tested materials relative to heat flux at various mass flux. At relatively low mass flow, two-phase boiling heat transfer coefficients of tested materials show wide variation, which cannot be observed at relatively high mass flow. It clearly demonstrates reducing material-sensitivity on boiling heat transfer coefficient with increasing flow rate.

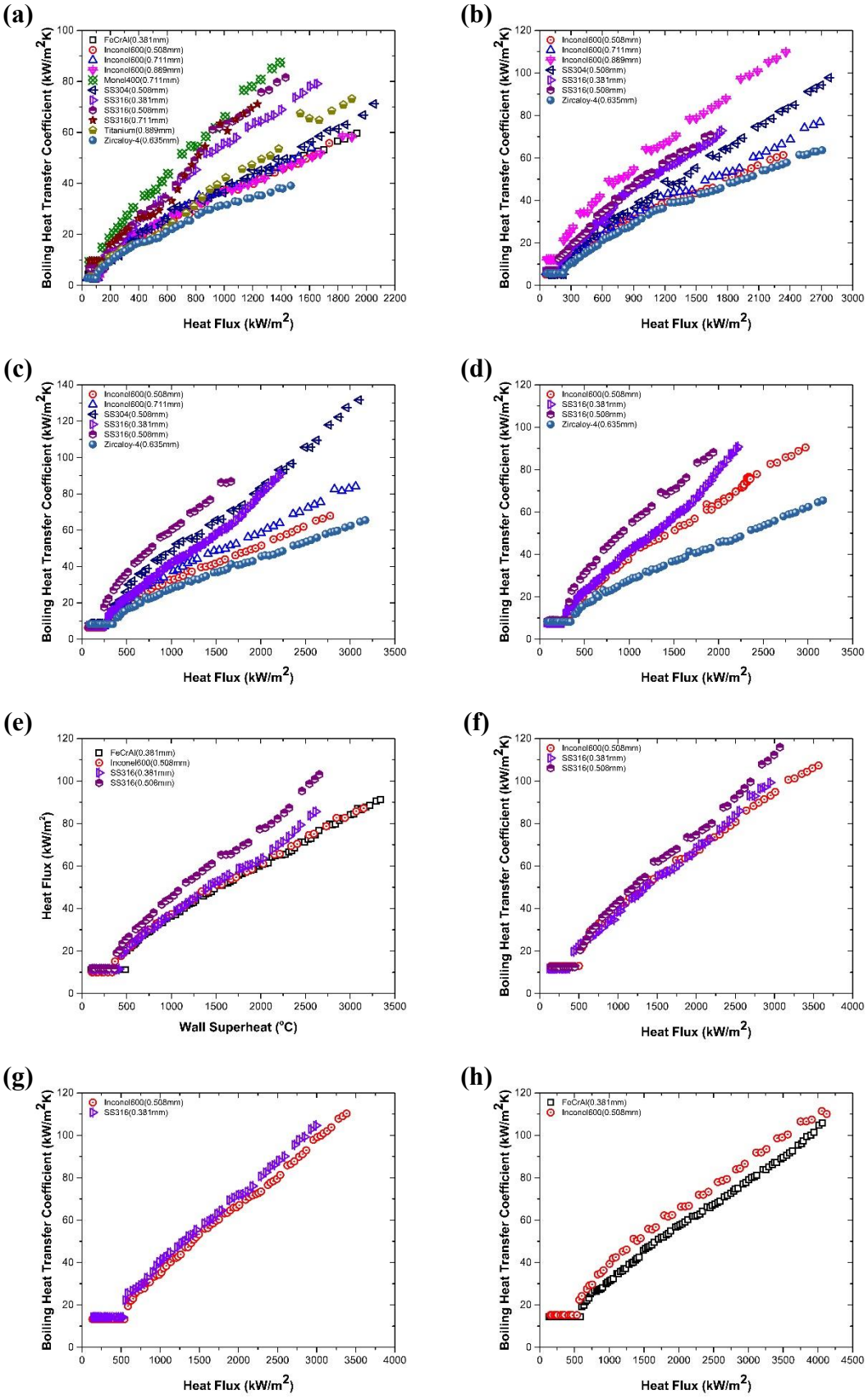

Figure 4.8 Boiling heat transfer coefficient in respect to measured heat flux of tested tube materials at mass flux (a) 200 kg/m^2s, (b) 400 kg/m^2s, (c) 600 kg/m^2s, (d) 800 kg/m^2s, (e) 1000 kg/m^2s, (f) 1200 kg/m^2s, (g) 1400 kg/m^2s, and (h) 1500 kg/m^2s (85kPa, 10℃ inlet subcooling)

Materials exhibit different CHF and boiling heat transfer rates in all tested flow conditions. At a low flow rate, considerable differences are observed. Yet, at a high flow rate, the relative boiling heat transfer coefficient difference decreases with flow rate. For accident progression, at a low flow rate, material-sensitivity may hold some importance considering observed differences among the tested materials. However, for fuel design and steady-state safety margin, material-sensitivity may have limited significance.

CHAPTER 5. OXIDIZED FeCrAl CHF STUDY

5.1 Steady-state CHF Results for Oxidized FeCrAl

I have submitted results in this chapter for journal publication [41]. The boiling behavior of fresh and oxidized FeCrAl (C26M) alloys was examined by steady-state CHF experiments under identical flow condition and compared to each other. Two FeCrAl alloy tubes were oxidized under hydrogen water chemistry autoclave exposure (150 ppb H_2, 288°C) and removed after 500 hour and 1000 hour respectively. In this study, two oxidized FeCrAl alloy tubes were compared to as-received fresh FeCrAl alloy tube under the steady-state flow boiling condition.

Boiling experiments were conducted at a fixed 2000 kg/m^2s mass flux and 10°C inlet subcooling under atmospheric pressure for all three tubes. Fig 5.1 presents the boiling curves of three tested FeCrAl alloy tubes obtained by the steady-state experimental data up to the CHF point under the reference flow condition. All three tubes show similar boiling behavior up to the onset of nucleate boiling (ONB), having almost identical single phase heat transfer coefficients. After the ONB, the oxide layer on the boiling surface affects the nucleate boiling heat transfer coefficients. 1000 hour oxidized surface demonstrates deteriorated nucleate boiling heat transfer compared to the 500 hour oxidized surface and fresh surface. Detailed analysis of boiling heat transfer coefficients is address in a later section. All three surfaces generated comparable steady-state CHF values under the reference flow condition. The absolute percent difference among tested surfaces is less than 1.8%, implying the limited effect of the oxide layer on steady-state

CHF under the tested condition. The surfaces with longer hydrogen water chemistry exposure induced higher wall superheat at the CHF occurrence and deteriorated nucleate boiling heat transfer.

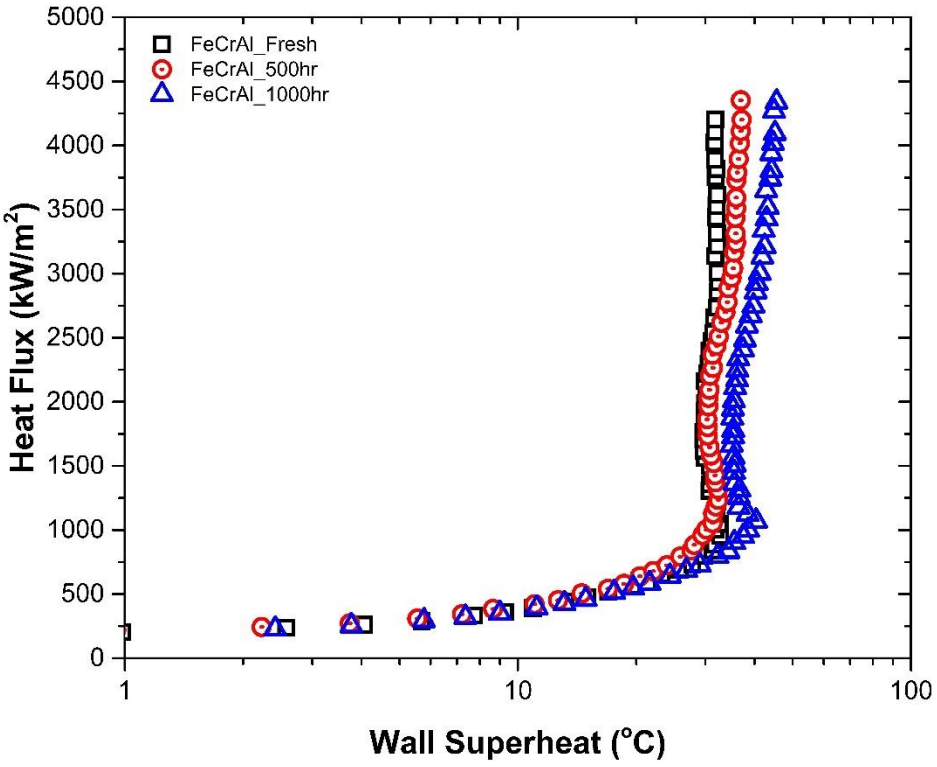

Figure 5.1 Steady-state flow boiling curve of as-received (fresh), 500 hour and 1000 hour oxidized FeCrAl (C26M) alloys at mass flux 2000 kg/m^{2}s (84kPa, 10°C inlet subcooling)

5.1.1 Surface Morphology Analysis

Surface morphology analysis was conducted to confirm oxide layer formation and to analyze changes of surface characteristics, which may affect boiling heat transfer.

Surface wettability and roughness were measured on each tested surface prior to the experiments. Scanning electron microscopy (SEM) and atomic force microscopy (AFM) images were taken to investigate morphology differences among reference surfaces.

Measured surface wettability in contact angle with measurement standard deviations are 57.75° ± 15.59°, 121.60° ± 4.00°, and 125.10° ± 2.16° for fresh, 500 hour and 1000 hour oxidized surfaces, respectively. Contact angle measurements clearly demonstrated a reduced affinity for water droplet due to the oxide layer on the FeCrAl surfaces. However, no significant wettability difference was observed for 500 hour and 1000 hour oxidized surfaces.

Measured surface roughness with standard deviations are 1.02 μm ± 0.23 μm, 1.55 μm ± 0.36 μm, and 1.23 μm ± 0.25 μm for as-received, 500 hour and 1000 hour oxidized surfaces, respectively. Surface roughness measurements done by stylus profilometer demonstrated slightly increased surface roughness on oxidized surfaces compared to the fresh surface. While surface wettability shows a drastic difference between fresh and oxidized surfaces, measured CHFs on each surface have no significant difference under the reference flow condition.

Scanning electron microscopy (SEM) images are shown in Fig 5.2. The SEM observation of FeCrAl surfaces prior to steady-state CHF experiments clearly show differences among the fresh, 500 hour and 1000 hour oxidized surfaces. Oxidized surfaces clearly show crystalline structure formation while as-received fresh FeCrAl surface shows no sign of any structure formation.

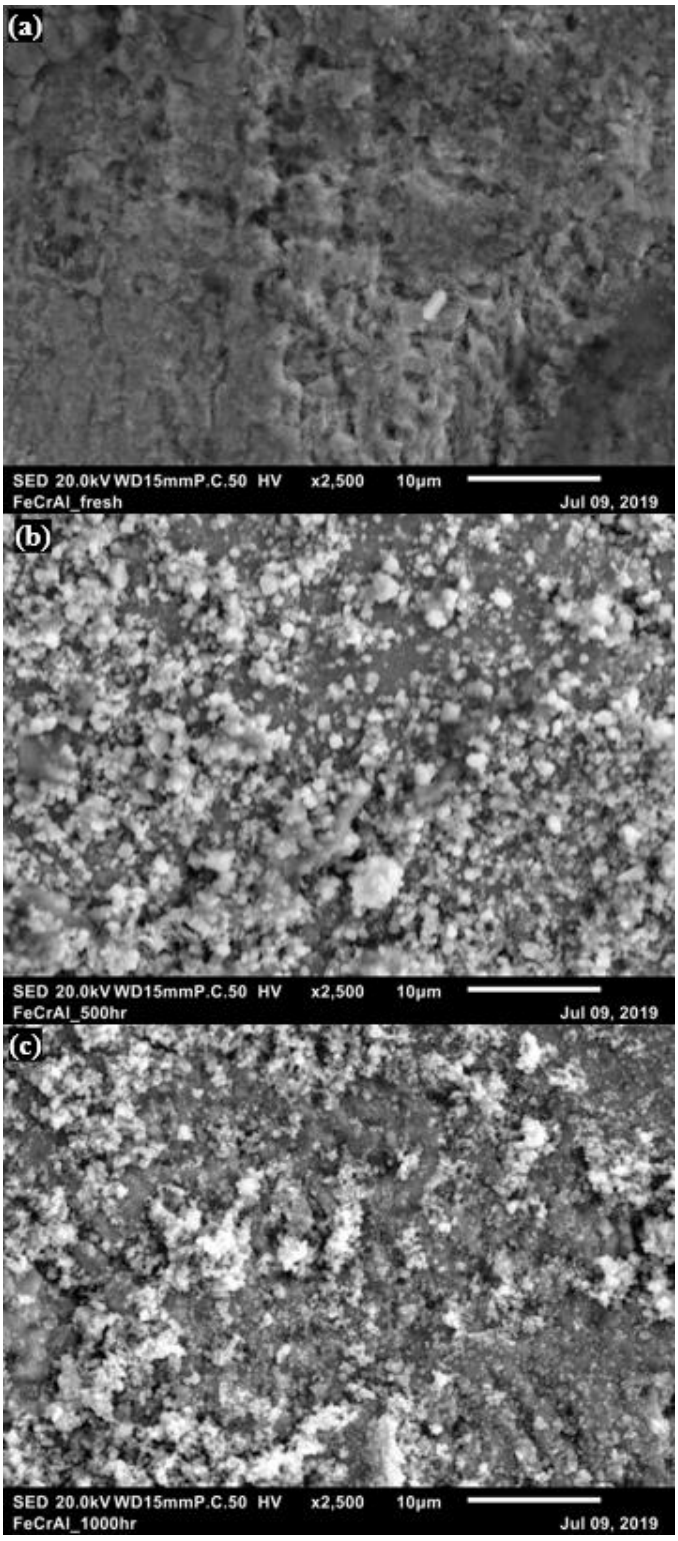

Figure 5.2 SEM micrograph of FeCrAl alloy inner surface in (a) as-received (fresh), (b) after 500 hour and (c) after 1000 hour hydrogen water chemistry autoclave exposure

Atomic force microscopy (AFM) topography images of as-received fresh, 500 hour and 1000 hour oxidized surfaces are shown in Fig 5.3. As it can be seen in Fig 5.3, examined FeCrAl surfaces show increasing height variation in increasing hydrogen water chemistry exposure period. Topography analysis from the collected data confirms an enlarged true area for oxidized FeCrAl surfaces compared to the as-received surface. True areas of measurements are 26.48 μm^2, 30.76 μm^2, and 32.38 μm^2 for as-received, 500 hour and 1000 hour oxidized surfaces, having identical reference area of 24.81 μm^2. AFM topography analysis provides arithmetic mean roughness, which are 154.27nm, 180.04nm, and 241.78nm for as-received, 500 hour and 1000 hour oxidized surfaces, respectively. Unlike the surface roughness measurement of stylus profilometer, AFM topography roughness analysis presents a clear positive relation between surface roughness to hydrogen water chemistry exposure period. Yet, under the tested flow condition, surface roughness has an insignificant relation to steady-state CHF.

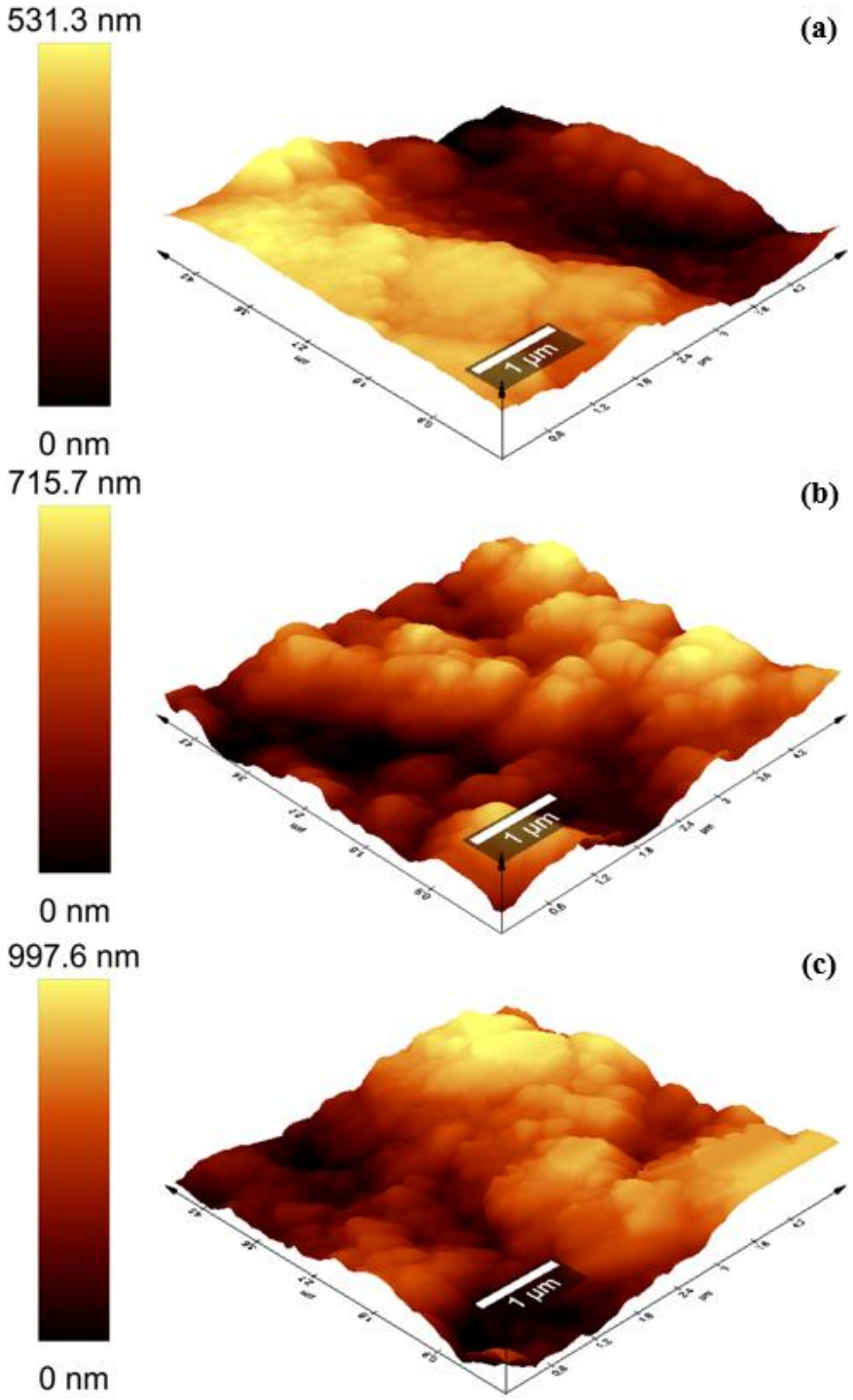

Figure 5.3 AFM topography of FeCrAl alloy inner surface in (a) as-received (fresh), (b) after 500 hour and (c) after 1000 hour hydrogen water chemistry exposure

5.1.2 Boiling Heat Transfer Analysis

Under the tested condition, the material with the longest autoclave exposure showed the lowest boiling heat transfer coefficient out of three. While surface roughness is known to have a positive relation to boiling heat transfer due to an increased number of active nucleation sites, a material with the lowest surface roughness (as-received fresh surface) was observed with the highest heat transfer coefficient in nucleate boiling regime. This result suggests that the development of the oxide layer deteriorates nucleate boiling heat transfer of given material. It is presumed that oxide layer prevents heat transfer between the working fluid and the heated material, leading boiling heat transfer coefficients to be reduced. Yet, reduced heat transfer coefficient from oxidized surface did not lead to any significant change in CHF, which again shows the limited significance of oxide layer on flow boiling CHF.

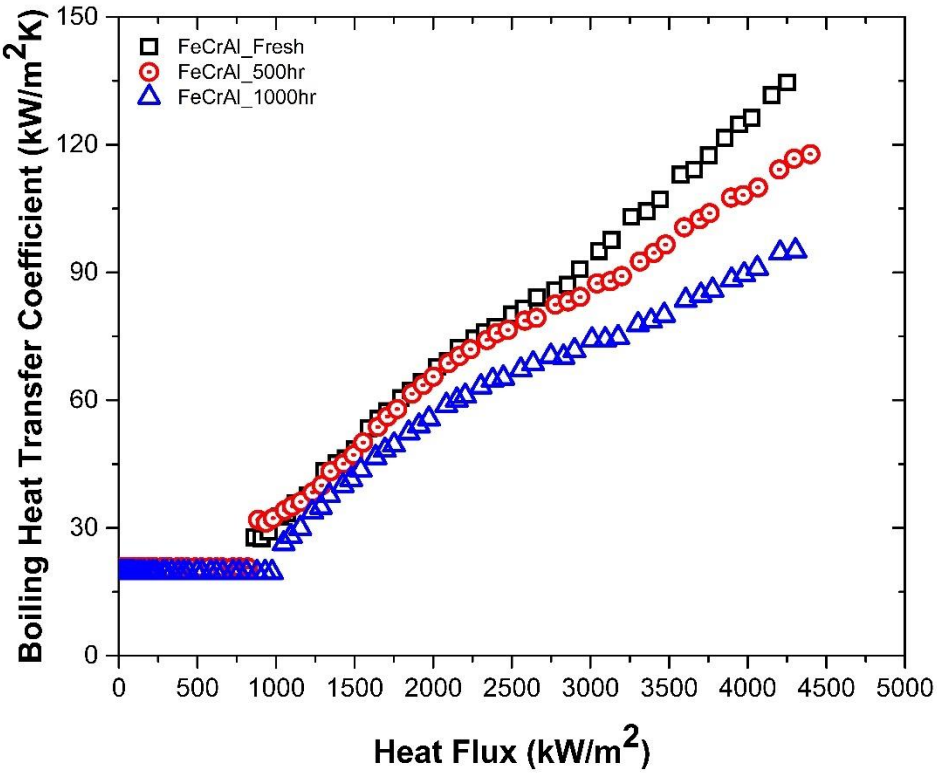

Figure 5.4 Heat transfer coefficient relative to heat flux on as-received (fresh), 500 hour and 1000 hour oxidized FeCrAl (C26M) alloys at mass flux 2000 kg/m^2s (84kPa, 10°C inlet subcooling)

CHAPTER 6. TRANSIENT CHF STUDY

6.1 Transient CHF Results

I have published results in this chapter [39, 43]. Transient CHF experiments were conducted on FeCrAl (C36M) alloy and Inconel 600 under atmospheric pressure. CHF experiment on FeCrAl (C36M) alloy was conducted at the same flow condition with the subcooled steady-state CHF experiment done in chapter 2. Thermodynamic quality at the instance of steady-state DNB was set as the inlet quality for a transient experiment, assuming thermodynamic quality does not change upon transience. By matching the thermodynamic quality, an impartial comparison was made between the steady-state and transient CHF under identical flow condition. The half sine shaped pulsed power with a peak of 5.8 MW/m^2 is applied for 1 second. In the case of Inconel 600 tubes, CHF experiments were conducted at a fixed 10℃ inlet subcooling with increasing mass flux from 200 kg/m^2s to 600 kg/m^2s. The half sine shaped pulsed power with a peak of 2.26 MW/m^2 is applied for 1 second in the heated length.

Table 6.1 Transient flow boiling CHF test condition

	Pressure	Mass Flux	Inlet Subcooling	Input Power
FeCrAl (C36M, 0.381mm)	84 kPa	300 kg/m^2s	3℃ (-0.0068)	Half sine shaped pulsed power 5.8MW/m^2 peak, 1s width
Inconel600 (0.508mm)	84 kPa	200 ~ 600 kg/m^2s	10℃	Half sine shaped pulsed power 2.7MW/m^2 peak, 1s width

To obtain transient CHF value, the transient energy balance equation is used to quantify heat flux applied for boiling and the implicit finite difference method is used to calculate inner surface temperature. The transient energy balance is shown as follows:

$$q''_{Transient\ CHF} = (Q - M \cdot c_p \cdot \frac{dT}{dt})/A_{inner} \tag{6.1}$$

To obtain the inner surface temperature, 1-D transient radial conduction equation is employed as follows:

$$\frac{1}{r} \cdot \frac{d}{dr} \cdot \left(k \cdot r \cdot \frac{\partial T}{\partial r}\right) + \dot{q} = \rho \cdot c_p \cdot \frac{\partial T}{\partial t} \tag{6.2}$$

The heat flux attained from the transient energy balance equation and measured outer surface temperature are used as the Neumann boundary condition. The implicit finite difference method (FDM) is adopted with boundary conditions. The following equations for discretized nodes account radial heat conduction, heat generation, and time rate change of the heat transfer on each node as shown in Fig 6.1(b).

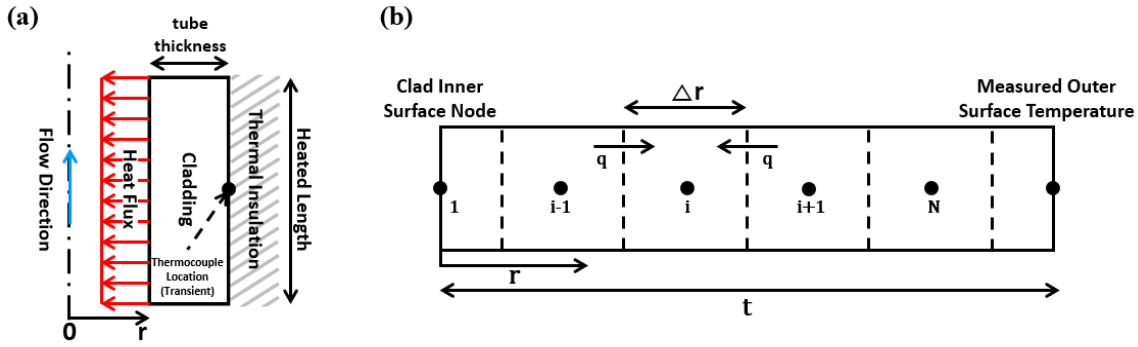

Figure 6.1 (a) Schematic of energy balance in heated wall (b) heater wall nodalization for inner surface temperature analysis

Inverse matrix operator A^{-1} in $A \cdot \vec{x} = b$ is used to solve following equations:

Cladding inner surface node, $i = 1$

$$-q''_{RIA}A_1 + \frac{k}{\Delta r}(T_2^{P+1} - T_1^{P+1})A_2 + Q^{P+1}\frac{V_1}{V_{tot}} = \rho c_p V_1 \frac{T_1^{P+1} - T_1^P}{\Delta t} \quad (6.3)$$

Cladding inner node, i

$$\frac{kA_{i-1}}{\Delta r}\left(T_{i-1}^{P+1} - T_i^{P+1}\right) + \frac{kA_{i+1}}{\Delta r}\left(T_{i+1}^{P+1} - T_i^{P+1}\right) + Q^{P+1}\frac{V_i}{V_{tot}} = \rho c_p V_i \frac{T_i^{P+1} - T_i^P}{\Delta t} \quad (6.4)$$

Cladding outer node, $i = N$

$$\frac{kA_{N-1}}{\Delta r}(T_{N-1}^{P+1} - T_N^{P+1}) + \frac{kA_N}{\Delta r}\left(T_{Measured}^{P+1} - T_N^{P+1}\right) + Q^{P+1}\frac{V_N}{V_{tot}} = \rho c_p V_N \frac{T_N^{P+1} - T_N^P}{\Delta t} \quad (6.5)$$

Fig 6.2 shows the calculated temperature distribution from the outer wall to the inner wall at DNB. The insulating condition of the outer surface is represented with the zero temperature gradient. The wall superheat at the transient CHF is approximately 30℃ higher compared to the wall superheat at the steady-state CHF under identical flow condition.

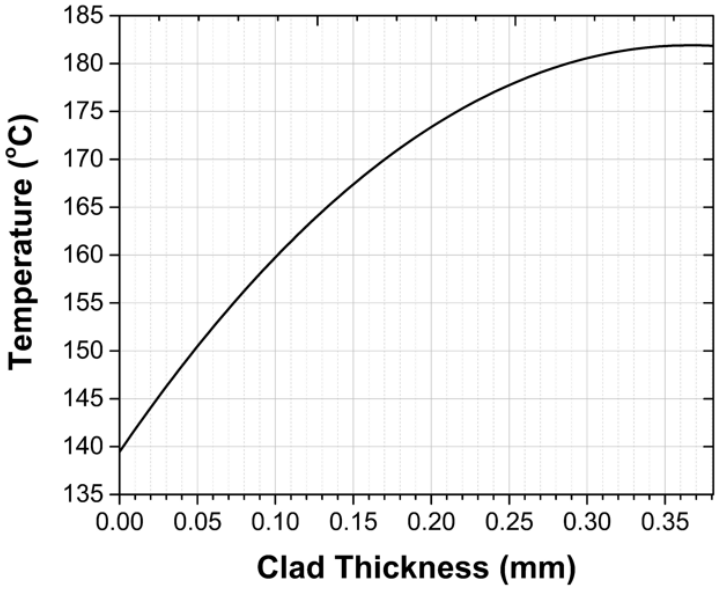

Figure 6.2 Temperature distribution along the radial axis of FeCrAl (C36M) alloy at DNB (applied power: half sine shaped pulsed power with 1 second width and 8088 Watts peak)

Experimental temperature and power measurements and post-experimental processed inner surface temperature and heat flux measurements are shown in Fig 6.3. Evaluated inner surface temperature from the FDM enables to identify the CHF and post-CHF boiling behavior including the rewetting point. In Fig 6.3(b), rapid temperature increase can be seen at 1.36 seconds compared to previous time steps, which corresponds to the CHF occurrence representing the transition of the boiling regime from the nucleate boiling to film boiling. After the CHF occurrence, the surface temperature increases very rapidly and decreases gradually, sustaining the vapor film along the heated length. Then, a point is reached where the vapor film no longer sustained, and the temperature drops rapidly. This point represents the rewetting point.

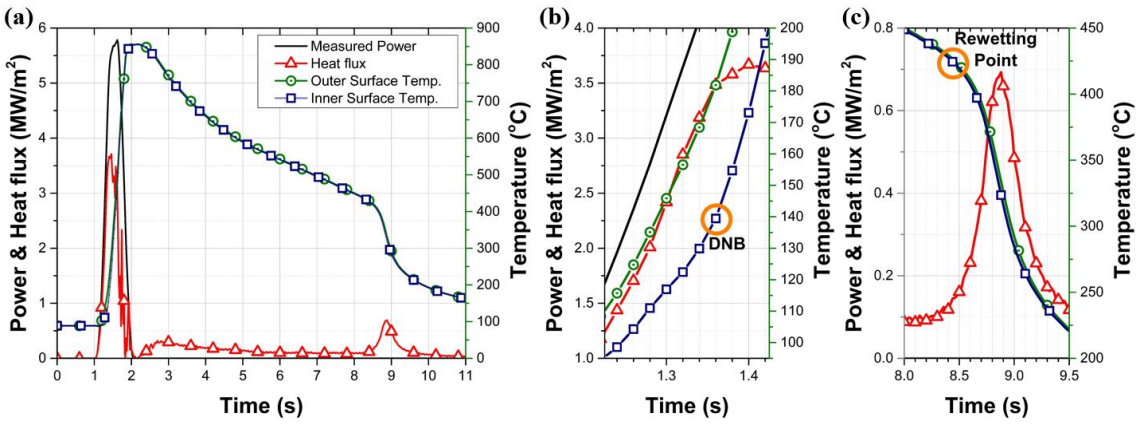

Figure 6.3 (a) Measured outer surface temperature and power and calculated inner surface temperature and heat flux for a transient CHF experiment ON FeCrAl (C36M)

alloy (Pulsed power: 1second width peak at 8088 Watts), (b) CHF determination, and (c) Rewetting point determination

Same experimental procedures were taken for FeCrAl alloy transient experiments by repeating identical experiments on the same tube sample to explore change in boiling behaviors due to surface condition change. As shown in Fig 6.4, transient CHF values and rewetting points do not change significantly with repeating experiments. It implies that surface change (i.e., oxide layer formation) has limited significance on transient CHF and rewetting point. Transient CHF induced the higher CHF value compared to the steady-state CHF under the identical flow condition. The transient CHF is shown to be 39% and 23% enhanced than the lookup table prediction and the steady-state CHF at given power input. Yet, transient CHF value may depend on the heating rate.

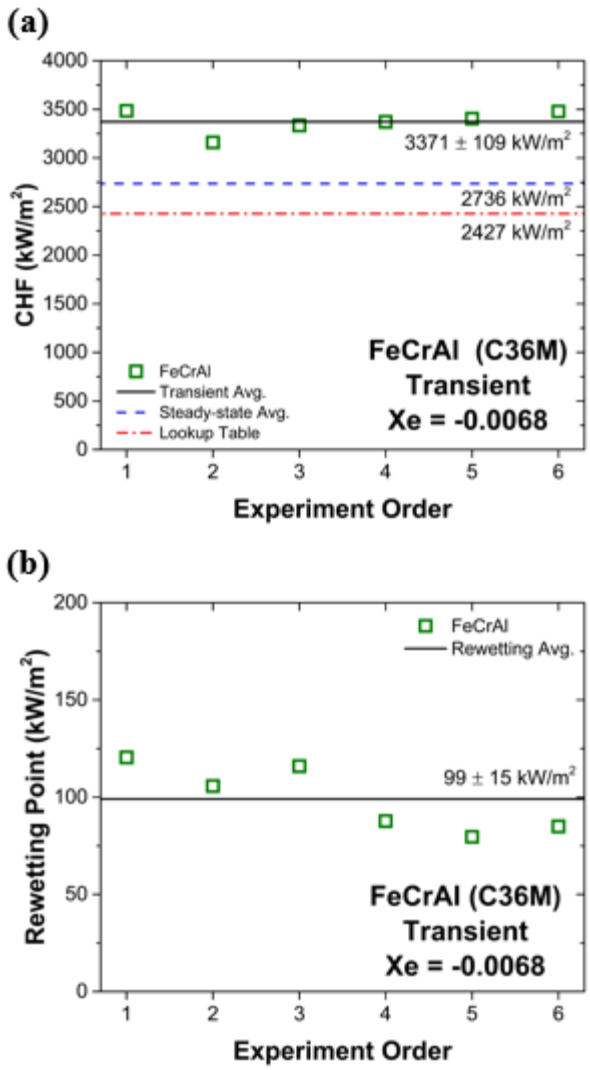

Figure 6.4 (a) Measured transient CHF data compared to the steady-state CHF data and the lookup table prediction (b) measured rewetting points of FeCrAl (C36M) alloy

In Fig 6.5, measurements of Inconel 600 transient boiling experiments are represented. For Inconel600, all experiments were conducted once on fresh tube samples. Identical post-experimental procedures are adopted to evaluate heat flux and inner wall surface temperature. For mass fluxes 200 kg/m^2s and 400 kg/m^2s, CHF was reached with the given power input, causing a temperature rise in the tube by the vapor film

formation. For 600 kg/m^2s mass flux, CHF was not reached due to fast cooling from the working fluid. Measured transient CHFs are 1.28 MW/m^2 and 1.85 MW/m^2 for 200 kg/m^2s and 400 kg/m^2s, respectively. Compared to the measured steady-state CHFs, transient CHFs showed no appreciable increase due to the relatively low heating rate.

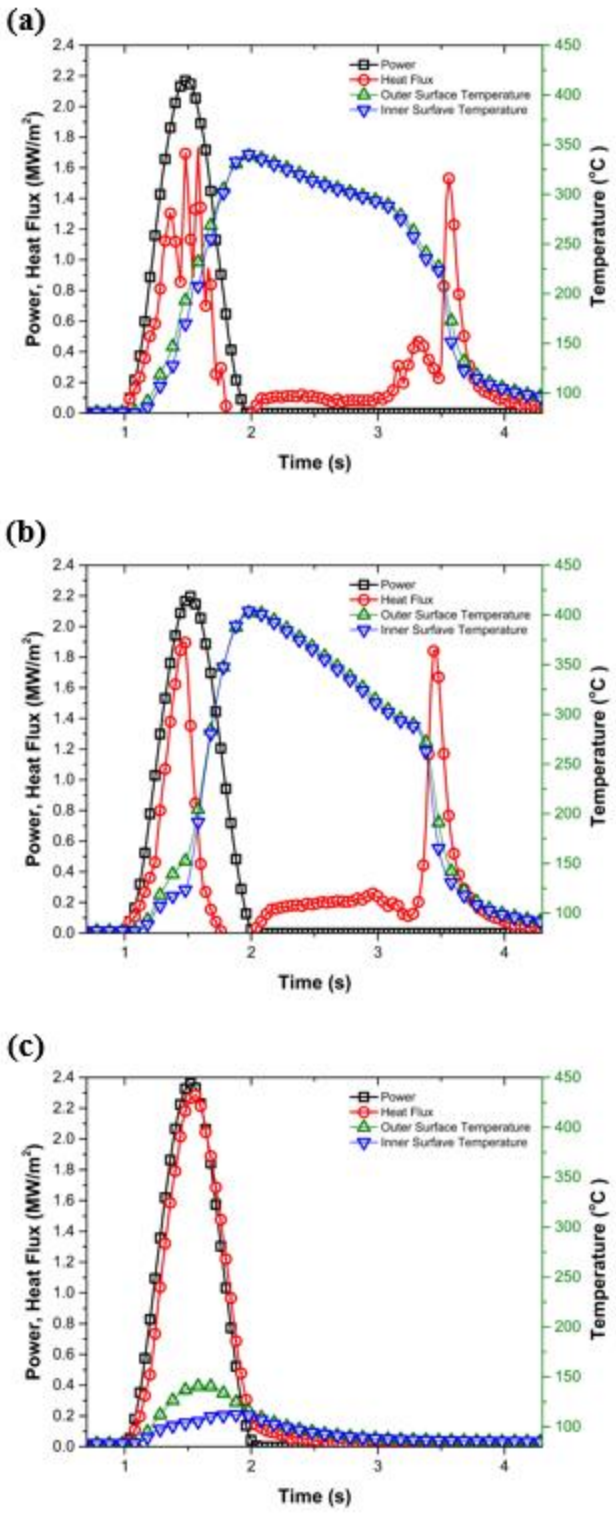

Figure 6.5 Transient boiling behavior measurements of Inconel600 at mass flux (a) 200 kg/m^2s, (b) 400 kg/m^2s, and (c) 600 kg/m^2s (84kPa, 10 inlet subcooling)

6.1.1 Transient Boiling Regime Analysis

In this section, a detailed analysis of transient boiling behavior is presented. In Fig 6.6, prototypical measurements of tube boiling behavior due to pulsed power input is shown. Measurements are divided into 6 different boiling regimes as follows:

① Single phase boiling regime: at the moment of the power insertion, single phase convection is sustained for short amount of time until it reaches the onset of nucleate boiling (ONB) as shown in Fig 6.6(b). ONB can be determined by the change of the temperature gradient, representing an increased heat transfer coefficient from bubble formation at the cavities.

② Nucleate boiling regime: nucleate boiling regime only sustained for 0.1 – 0.2 seconds and the departure of nucleate boiling (DNB) occurs to overshoot the inner wall surface temperature rapidly. It is due to the excessive amount of power input heating up the test tube in such a short time period. DNB can be determined by the rapid change of the temperature gradient with decreasing heat flux.

③ Transition boiling regime: once DNB is reached, vapor columns transition into vapor film, causing the rapid temperature to rise in the fluid–wall interface.

④ Film boiling regime: vapor film created by DNB is sustained until it reaches the rewetting point, which is characterized by the onset of sharp surface temperature decrease. The surface temperature at the rewetting point corresponds to the minimum film boiling temperature.

⑤ Transition boiling regime: right after the rewetting point, maximum attainable heat flux due to liquid quenching can be observed. It is characterized by the rapid rise of the

heat flux due to the recovery of heat transfer rate upon the transition from the film boiling region to nucleate boiling regime.

⑥ Single phase boiling regime: with no power insertion, boiling regime returns to the single phase convection and eventually cools down.

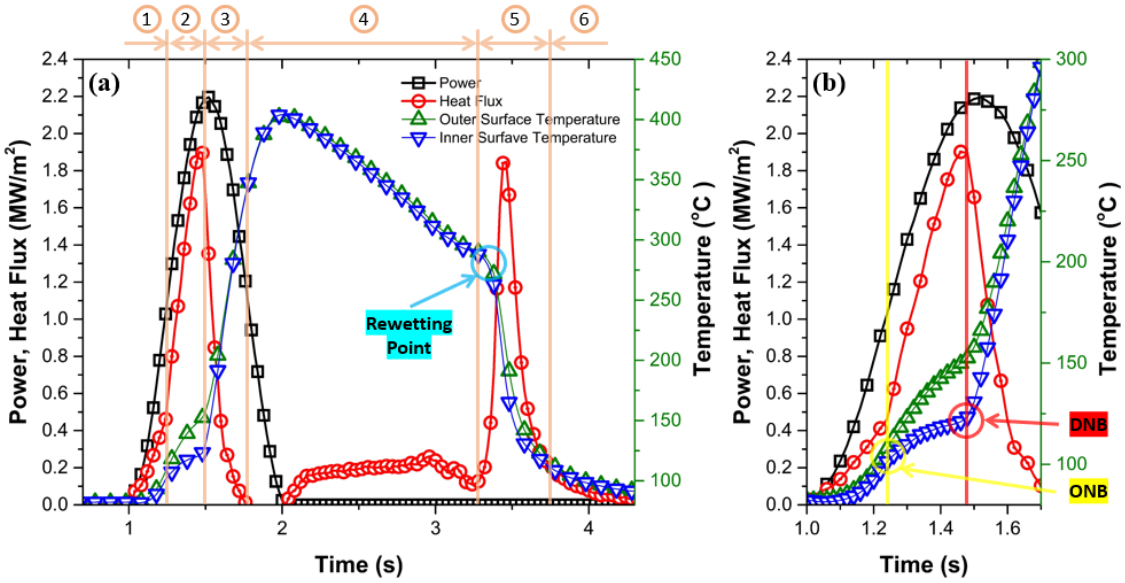

Figure 6.6 (a) Transient boiling behavior of Inconel600 at mass flux 400 kg/m^2s, (b) enlarged view at ONB and DNB

6.1.2 Transient Boiling Curve Construction

With an understanding of flow boiling regimes, detailed prototypical procedures for transient boiling curve construction is discussed in this section. This procedure is developed for potential implementation in the reactor safety analysis codes. Boiling curve construction is accomplished using experimentally measurable values (①-⑥ in Fig 6.7(b)) as follows:

① Transient ONB: transient ONB can be measured by inner wall surface temperature change right after the power insertion

② Transient CHF: transient CHF or DNB can be measured by inner wall surface temperature overshoot

③ Film boiling heat transfer coefficient, h_{film}: h_{film} can be obtained from the heat flux change rate relative to the cladding surface change in the film boiling regime, $\frac{\mathrm{dq}''}{dT_{surface}} = h_{film}$

④ Rewetting point: rewetting point is determined by the onset of sharp temperature decrease after the film boiling regime

⑤ Maximum attainable heat flux due to liquid quenching: it is characterized by the heat flux peak caused by the recovery of heat transfer rate upon the transition

⑥ Onset of single phase convection: it is characterized by the rate of heat flux decrease relative to the rate of temperature decrease soon after point ⑤.

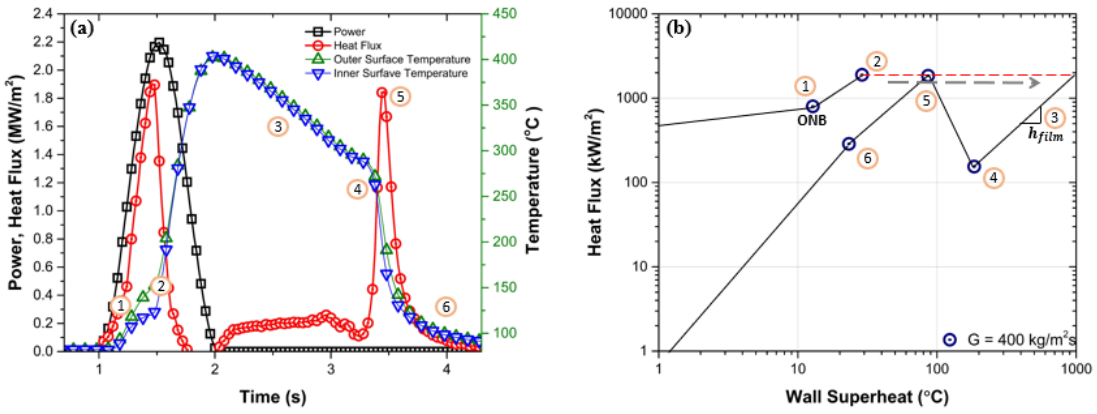

Figure 6.7 Transient flow boiling curve for Inconel600 at mass flux 400 $\mathrm{kg/m^2 s}$ (84kPa, 10 inlet subcooling)

Following the above procedure, the transient flow boiling curve for FeCrAl (C36M) alloy is constructed with a steady-state flow boiling curve in Fig 6.8. Yet, in the FeCrAl alloy transient CHF experiment, ONB was not detected due to excessive power input and slow sampling rate.

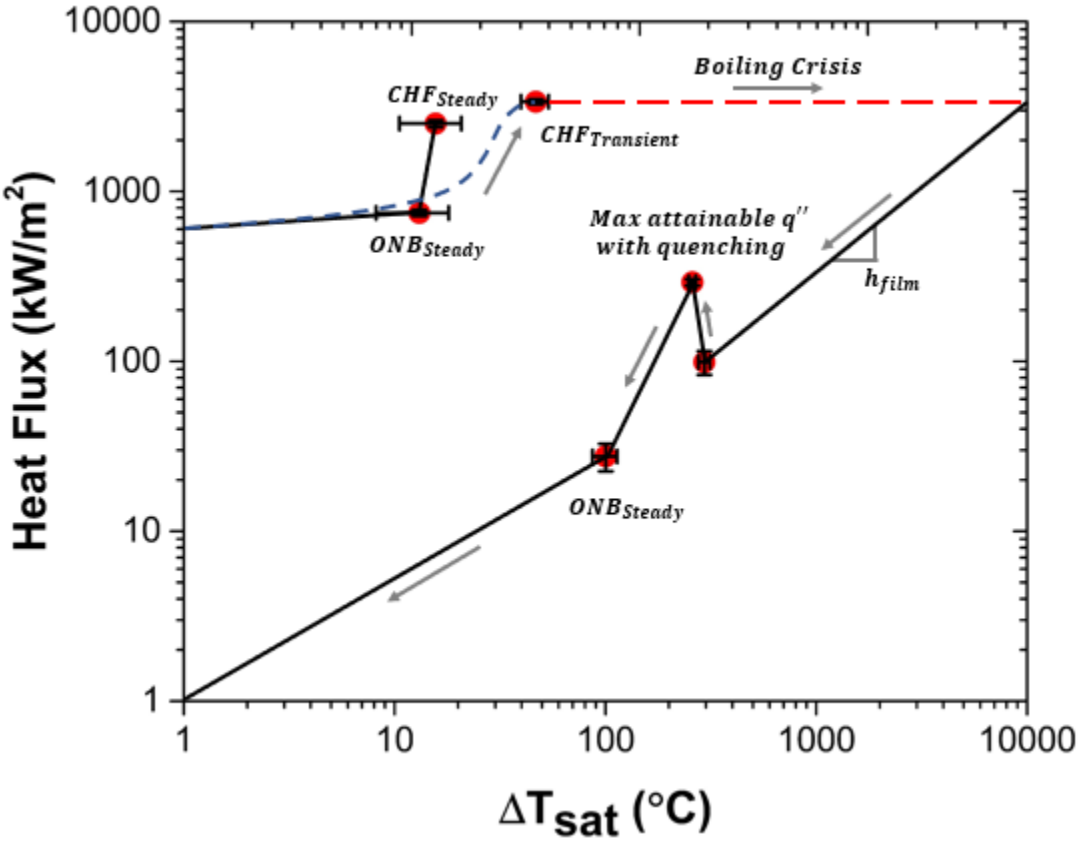

Figure 6.8 Transient flow boiling curve of FeCrAl (C36M) alloy at mass flux 300 kg/m^{2}s (84kPa, quality at -0.0068)

6.1.3 Effect of Mass Flow on Transient CHF

In Fig 6.9, boiling curves of Inconel 600 under two flow conditions are shown. Identical power input was applied to investigate the effect of mass flux on transient CHF. A higher mass flux induced increased ONB and DNB at the higher superheat. Moreover, the measured film boiling heat transfer coefficient is higher due to the increased heat transfer capability from the increased mass flow. This result implies that transient boiling behavior can be significantly influenced by the flow condition, thereby experimental data is required for transient behavior safety analysis.

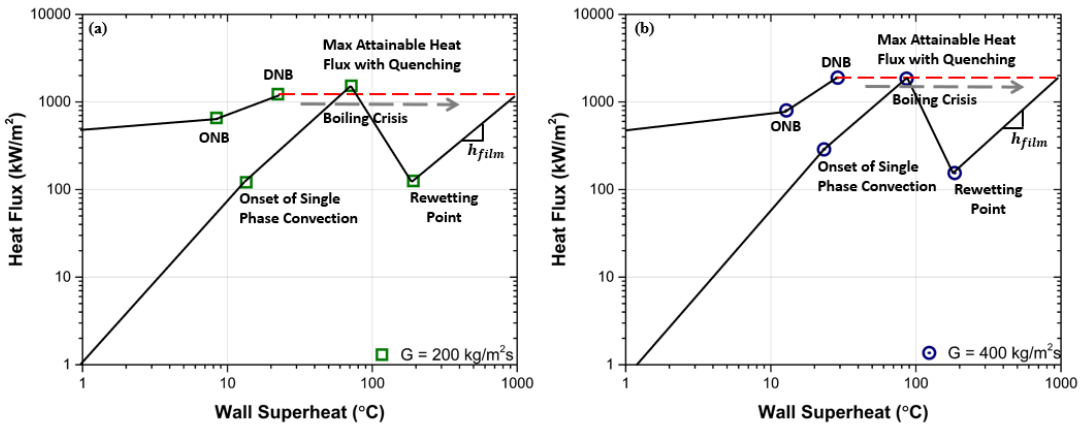

Figure 6.9 Transient boiling curve of Inconel600 at mass flux (a) 200 kg/m^2s and (b) 400 kg/m^2s (84kPa, 10℃ inlet subcooling)

Chapter 6 Nomenclature

$q''_{Transient\ CHF}$	Transient Critical Heat Flux
Q	Applied heat generation rate in the heated length
M	Mass of the heated test section
c_p	Specific heat of the test material
dT	Change in temperature
dt	Change in time step
A_{inner}	Boiling surface area
r	Radius
P	Time step
T	Temperature
A	Area
V	Volume

CHAPTER 7. CONCLUSIONS

7.1 Conclusions

In this study, steady-state and transient internal flow CHF experiments were carried out under atmospheric pressure covering a wide range of mass flux (200 kg/m^2s - 2000 kg/m^2s) on various tube materials including FeCrAl accident tolerant fuel cladding alloy. In the first part of the study, steady-state CHF experiments were carried out on FeCrAl (C36M) alloy, Zircaloy, and Inconel tubes under identical flow condition, investigating the effect of surface morphology change and thermal parameters on flow boiling CHF. In the second part of the study, the statistical analysis approach was made on various tube materials covering a wide range of mass flux, thereby investigating the effect of mass flow to understand observed CHF differences among various materials. Moreover, oxidized FeCrAl (C26M) alloy tubes under hydrogen water chemistry exposure were used to conduct steady-state CHF experiments to investigate boiling behavior. Lastly, transient CHF experiments were carried out on FeCrAl (C36M) alloy and Inconel tubes to analyze the cladding behavior under transient heat insertion. The following conclusions can be made:

1. In spite of the notable changes in surface wettability and surface roughness due to oxide layer formation, flow boiling CHF change to these parameters was not observed via repeated CHF experiments on FeCrAl (C36M) alloy, Zircaloy, and Inconel tubes. It implies that surface characteristics may have limited significance on flow boiling CHF under tested flow condition. Observed insignificance of surface characteristics may be limited to the current test set up.

2. Implications of material thermal parameters (thermal effusivity, thermal activity, thermal diffusivity, and surface thermal economy) on the flow boiling CHF were explained to understand observed CHF differences among the tested materials. Given the limited range of the material thermal parameters, no clear relation to measured CHFs were observed.

3. Experimental steady-state CHF data of various materials covering a wide range of mass flux were compared to each other, which showed reducing gaps among the different CHF attendants with increasing mass flux. The 2006 CHF lookup table was used as a frame of reference to compare apparent CHF differences, which also showed reducing gaps between the experimental data and the lookup table predictions relative to increasing mass flow. This result tentatively concludes the material sensitivity on CHF may decrease with increasing mass flow. Observed insignificance of material-sensitivity may be limited to the current test set up.

4. Experimental steady-state boiling curves of tested materials showed considerable differences at a relatively low flow rate; yet, the boiling heat transfer coefficient and CHF differences among the tested material decreased with respect the increase in flow rate. It implies that material-sensitivity may hold limited significance in fuel and cladding design and steady-state safety margin. Still, under the accident scenarios where mass flow is low, material effect on boiling heat transfer may play a big role as observed CHFs vary from different materials.

5. The oxidized FeCrAl alloy tubes under steady-state power increment visited very similar flow CHF compared to the as-received fresh FeCrAl alloy tube, representing

less than 1.8% difference. Yet, the nucleate boiling heat transfer efficiency was deteriorated due to the oxide layer formation on the heated surface.

6. Transient boiling CHF experiments were carried out and compared to the steady-state CHF data at the identical flow and DNB condition, which showed 39% and 23% increased value compared to the lookup table prediction and the steady-state CHF. Moreover, prototypical cladding heat transfer behavior upon the transient pulsed power insertion is analyzed to construct the transient boiling curve using experimentally measurable values.

REFERENCE

[1] A.W. Cronenberg, In-vessel Zircaloy oxidation/hydrogen generation behavior during severe accidents, NUREG/CR-5597. US NRC, Washington DC (1990).

[2] J. Carmack, K. Barret, and H. MacLean-Chichester, Light Water Reactor Accident Tolerant Fuels Irradiation Testing, INL/CON-15-34949, Idaho falls, ID (2015).

[3] K.A. Terrani, S.J. Zinkle, and L.L. Snead, Advanced oxidation resistant iron-based alloys for LWR fuel cladding, Journal of Nuclear Materials 448.1 (2014) 420-435

[4] K.A. Terrani, B.A. Pint, C.M. Parish, C.M. Silva, L.L. Snead, and Y. Katoh, Silicon carbide oxidation in steam up to 2 MPa, Journal of the American Ceramic Society 97,8 (2014) 2231-2352

[5] M.B. Cinbiz, N.R. Brown, R.R. Lowden, M.N. Gussev, K.D. Linton, K.A. Terrani, Report on Design and Failure Limits of SiC/SiC and FeCrAl ATF Cladding Concepts under RIA (No. ORNL/LTR- 2018/521). Oak Ridge National Laboratory, Oak Ridge, TN (2018)

[6] K.A. Terrani, T.M. Karlsen, Y. Yamamoto, Input correlations for irradiation creep of FeCrAl and SiC based on in-pile Halden test results, Technical Report ORNL/ TM-2016/191, Oak Ridge National Laboratory, 2016.

[7] K.A. Gamble, T. Barani, D. Pizzocri, J.D. Hales, K.A. Terrani, G. Pastore, An investigation of FeCrAl cladding behavior under normal operating and loss of coolant conditions, J. Nucl. Mater. 491 (2017) 55–66k.

[8] J.J. Powers, N.M. George, G.I. Maldonado, and A. Worrall, "Report on Reactor Physics Assessment of Candidate Accident Tolerant Fuel Cladding Materials in LWRs" (ORNL/TM-2015/415). Oak Ridge National Laboratory, Oak Ridge, TN (2015)

[9] N.M. George, K.A. Terrani, J. Powers, A. Worrall, I. Maldonado, Neutronic analysis of candidate accident-tolerant cladding concepts in pressurized water reactors, Ann. Nucl. Energy 75 (2015) 703–712.

[10] N.R. Brown, M. Todosow, A. Cuadra, Screening of advanced cladding materials and UN–U 3 Si 5 fuel, J. Nucl. Mater. 462 (2015) 26–42.

[11] N.R. Brown, A.J. Wysocki, K.A. Terrani, K.G. Xu, D.M. Wachs, The potential impact of enhanced accident tolerant cladding materials on reactivity initiated accidents in light water reactors, Ann. Nucl. Energy 99 (2017) 353–365.

[12] J.R. Burns, N.R. Brown, Neutron cross section sensitivity and uncertainty analysis of candidate accident tolerant fuel concepts, Ann. Nucl. Energy 110 (2017) 1249–1255.

[13] Y. Lee, J.I. Lee, H.C. No, Mechanical analysis of surface-coated zircaloy cladding, Nucl. Eng. Technol. 49 (2017) 1031–1043.

[14] Y. Lee, H.C. No, J.I. Lee, Design optimization of multi-layer silicon carbide cladding for light water reactors, Nucl. Eng. Des. 311 (2017) 213–223.

[15] Y. Lee, H.S. Kim, H.C. No, Failure probabilities of SiC clad fuel during a LOCA in Public Acceptable Simple SMR (PASS), Nucl. Eng. Des. 292 (2015) 1–16.

[16] Y. Lee, M.S. Kazimi, A structural model for multi-layered ceramic cylinders and its application to silicon carbide cladding of light water reactor fuel, J. Nucl. Mater. 458 (2015) 87–105.

[17] C. Han, P. Griffith, The mechanism of heat transfer in nucleate pool boiling, A technical report, Massachusetts Institute of Technology (1962).

[18] Y.Y. Hsu, On the size range of active nucleation cavities on a heating surface, Journal of heat transfer, (1962) 207-213

[19] V. Bessiron, Modelling of clad-to-coolant heat transfer for RIA applications, Journal of nuclear science and technology. 44 (2007) 211-221.

[20] V. Bessiron, T. Sugiyama, T. Fuketa, Clad-to-coolant heat transfer in NSRR experiments, Journal of nuclear science and technology. 44 (2007) 723-732.

[21] R. Visentini, C. Colin, P. Ruyer, Experimental investigation of heat transfer in transient boiling, Experimental thermal and fluid science 55 (2014) 95-105.

[22] G. Su, M. Bucci, T. McKrell, J. Buongiorno, Transient boiling of water under exponentially escalating heat inputs. Part II: flow boiling, International journal of heat and mass transfer. 96 (2016) 685-698.

[23] M. Liu, N.R. Brown, K.A. Terrani, A. Ali, E.D. Blandford, D.M. Wachs, Potential impact of accident tolerant fuel cladding critical heat flux characteristics on the high temperature phase of reactivity initiated accidents, Annals of nuclear engineering, 110 (2017) 48-62.

[24] D.C. Groeneveld, J.Q. Shan, A.Z. Vasic, L.K.H. Leung, A. Durmayaz, J. Yang, S.C. Cheng, A. Tanase, The 2006 CHF look-up table, Nuclear engineering and design, 237 (2007) 1909-1922.

[25] A. Ali, J. Gorton, N.R. Brown, K.A. Terrani, C. Jensen, Y. Lee, E.D. Blandford, Surface wettability and pool boiling critical heat flux of accident tolerant fuel cladding FeCrAl alloys, Nuclear engineering and design, 338 (2018) 218-231.

[26] V. K. Dhir and S. P. Liaw, Framework for a unified model for nucleate and transition pool boiling, Journal of Heat Transfer, 111 (1989) 739

[27] S.G. Kandlikar, Critical heat flux in subcooled flow boiling – An assessment of current understanding and future directions for research, Multiphase Science and Technology, 13 (2001) 105-130.

[28] H. O'Hanley, C. Coyle, J. Buongiorno, T. McKrell, L.W. Hu, M. Rubner, R. Cohen, Separate effects of surface roughness, wettability, and porosity on the boiling critical heat flux, Applied physics letters, 103 (2013) 024102

[29] H.S. Ahn, H. Kim, H. Jo, S.H. Kang, W.P. Chang, M.H. Kim, Experimental study of critical heat flux enhancement during forced convective flow boiling of nanofluid on a short heated surface, international journal of multiphase flow, 36 (2010) 375-384

[30] M.H. Lee, H. Heo, I.C. Bang, Effect of thermal activity on critical heat flux enhancement in downward-hemispherical surface using graphene oxide coating, International journal of heat and mass transfer, 127 (2018) 1102-1111

[31] G.H. Seo, G. Jeun, S.J. Kim, Enhanced pool boiling critical heat flux with a FeCrAl layer fabricated by DC sputtering, International journal of heat and mass transfer, 102 (2016) 1293-1307

[32] Y. Yamamoto, B.A. Pint, K.A. Terrani, K.G. Field, Y. Yang, L.L. Snead, Development and property evaluation of nuclear grade wrought FeCrAl fuel cladding for light water reactors, Journal of nuclear materials, 467 (2015) 703-716

[33] American Society of Testing Materials (ASTM), Standard Practice for Surface Wettability of Coatings, Substrates and Pigments by Advancing Contact Angle Measurement, Designation: D7334 – 08 (2013)

[34] T.L. Bergman, A.S. Lavine, F.P. Incropera, D.P. Dewitt, Fundamentals of heat and mass transfer, seventh edition, John Wiley & Sons, Inc, Hoboken, NJ, USA, 2011

[35] M. Arik, A. Bar-Cohen, Effusivity-Based Correlation of Surface Property Effects in Pool Boiling CHF of Dielectric Liquids, International Journal of Heat and Mass Transfer, 46 (2003) 3755-3764

[36] I. Golobič, A.E. Bergles, Effects of Heater-Side Factors on the Saturated Pool Boiling Critical Heat Flux, Experimental Thermal and Fluid Science, 15 (1997) 43-51

[37] G. Guglielmini, E. Nannei, On the Effect of Heating Wall Thickness on Pool Boiling Burnout, International Journal of Heat and Mass Transfer, 19(1976) 1073-1075

[38] I.I. Gogonin, "Influence of the Thickness of a Wall and of its Thermophysical Characteristics on the Critical Heat Flux in Boiling," Journal of Engineering Physics and Thermophysics, 82 (2009) 6

[39] S.K. Lee, M. Liu, N.R. Brown, K.A. Terrani, E.D. Blandford, H. Ban, C.B. Jensen, and Y. Lee, Comparison of steady and transient flow boiling critical heat flux for FeCrAl accident tolerant fuel cladding alloy, Zircaloy, and Inconel, International Journal of Heat and Mass Transfer 132 (2019) 643-654

[40] S.K. Lee, N.R. Brown, K.A. Terrani, Y. Lee, Experimental investigation of steady-state flow boiling critical heat flux with various tube materials, Submitted to International Journal of Heat and Mass Transfer

[41] S.K. Lee, N.R. Brown, K.A. Terrani, Y. Lee, Steady-state flow boiling critical heat flux of oxidized Accident Tolerant Fuel cladding – FeCrAl alloy, Submitted to Nuclear Engineering and Design

[42] S.K. Lee, M. Liu, N.R. Brown, K.A. Terrani, Y. Lee, Effect of heater material and thickness on the steady-state flow boiling Critical Heat Flux, Submitted to Nuclear Technology

[43] S.K. Lee, N.R. Brown, K.A. Terrani, C.B. Jensen, H. Ban, Y. Lee, Study of transient CHF and post-CHF flow boiling, 18th International Topical Meeting on Nuclear Reactor Thermal Hydraulics (NURETH-18), Portland, OR, August 18-23, 2019.